Devlopment of Germanium thin films for solar cell fabrication

Shubham N. Litke



Delft University of Technology

TU Delft

Devlopment of Germanium thin films for solar cell fabrication

by

Shubham N. Litke

Student Name

Shubham N. Litke

Supervisor:	Dr. Arno Smets
Daily supervisor:	Dr. Paula Perez Rodriguez
PVMD examiner:	Dr. Moumita Rana
External examiner:	Dr. Hani Vahedi
Project Duration:	Novemeber, 2023 - August, 2024
Faculty:	Faculty of Electrical Engineering, Mathematics and Computer Science, Delft

Style: TU Delft Report Style, with modifications by Daan Zwaneveld

TU Delft

Acknowledgements

This thesis has been a culmination of many challenges that have shaped me both personally and professionally. I would like to extend my gratitude to all those who have supported me throughout this journey.

First and foremost, I would like to thank my parents and my brother for their unwavering belief in me. Their love and support have been my rock, guiding me through the toughest situations. My parents have always been my biggest cheerleaders, encouraging me to pursue my dreams and never give up, no matter the obstacles. I owe them more than words can express.

I extend my heartfelt thanks to my friends, both in the Netherlands and in India, for their unceasing acknowledgement and companionship. Furthermore, I would like to especially thank Shreya Kejriwal, Rupesh Yellamraju, Divye Kanawala, Zeba Rehaman, Neel Lodha, Abhiroop Bhowmik, Manali Shah, Samarth Trichy, Anand Mahajan for their continuous support and encouragement. Each of you has been a constant source of motivation, sharing in my struggles and triumphs, whether from the Netherlands or India. Your friendship has been invaluable throughout this journey, reminding me that I never walk alone.

I would also like to express my sincere gratitude to my mentors, Dr. Paula Perez and Dr. Arno Smets. Their invaluable guidance, expertise, and patience have been instrumental in shaping my work and pushing me to think critically and proactively. I am deeply appreciative of their support, especially during moments when the outcomes were not as expected. Their encouragement to persist and keep learning from every challenge has been crucial to my growth.

A special thanks also goes to the lab technicians, whose expertise and dedication ensured the smooth operation of the lab facilities. Their behind-the-scenes support often went unnoticed but was critical to the success of my research, and I am truly grateful for their efforts.

This journey has been a profound learning experience, one that has deepened my understanding of the subject and provided me with lessons in resilience, patience, and perseverance. These lessons will stay with me as I move forward in my career and life, and I will always cherish this time of growth.

As I finish this chapter, I am excited about the future and the new challenges and opportunities it will bring. I look forward to using the knowledge and skills I've gained and growing in both my personal and professional life.

Shubham N. Litke
Delft, September 2024

Abstract

This thesis aimed to process and characterize hydrogenated germanium (Ge:H) films to use them as a low-bandgap intrinsic absorber layer. The bandgap of Germanium can go down to 0.67 eV. A p-i-n solar cell consisting of intrinsic germanium film produced using Plasma Enhanced Chemical Vapour Deposition (PECVD) can be inexpensively paired with crystalline silicon and other semiconductor materials to produce a multi-junction solar cell with high efficiencies. Such a cell would utilize the lower part of the solar spectrum currently untapped in commercially available mass-produced solar modules. Previous research had deposited Ge:H films using a counterflow PECVD reactor, as compared to a showerhead configuration in the reactor used in this research.

The study consisted of experiments that explored the properties of the germanium film deposited. First, the deposition parameters of PECVD were varied to study its effect on important film properties. Since the germanium layer will be used in a solar cell as the absorber layer, the band-gap and activation energy were the most critical parameters to monitor film intrinsicity. Experiments were performed by depositing germanium layers on glass substrates and silicon wafers to understand the properties of the films when deposited at different temperatures and also when the germane flow was altered. The effect of the power and pressure on the properties of the germanium samples was studied too. In all these experiments, the deposition time and electrode gap are kept constant. The processing window of 3-4.5 mbar and 12-20 W where intrinsic amorphous germanium (a-Ge:H) films can be produced was identified.

Single junction solar cells in p-i-n and n-i-p configuration were then incorporated with the intrinsic amorphous germanium. The p-i-n configuration displayed solar cell characteristics, whereas the n-i-p configuration cells did not, despite the changes in doping of the p-layer. Further experiments were carried out to look into the stability of the material by repeating the J-V curve measurement of the first cell that showed solar cell characteristics, but similar

behaviour was not observed. Additionally, Raman spectroscopy was carried out, which revealed that the material is amorphous.

In summary, the results look promising in proving these films as a suitable material for an intrinsic absorber layer. It also strongly suggests that the showerhead PECVD configuration can lead to better control of reaction mechanics, giving films with desired material properties. The layer can be used as an intrinsic layer in a p-i-n structure device, but further investigation is required to look into the interaction of the layers of the solar cells.

Contents

Acknowledgements **i**

Abstract **iii**

Nomenclature **xi**

1 Introduction **1**

1.1 Research objectives and outline 3

2 Background **4**

2.1 Solar energy 4

2.2 Semiconductor properties 6

2.2.1 Germanium properties 8

2.3 Recombination mechanisms and losses 10

2.4 Photovoltaic technologies 12

2.4.1 Generation of solar cells 13

2.5 Single junction solar cell 14

2.5.1 p-i-n junction 14

2.6 Multi-junction solar cell devices 16

2.6.1 Solar cell performance 18

3 Methodology **21**

3.1 Processing techniques and equipment 21

3.1.1 Substrate preparation 21

3.1.2 Plasma Enhanced Chemical Vapour Deposition (PECVD) 22

3.1.3 Germanium intrinsic layer deposition 24

3.1.4 Previous research and obtaining optimum conditions for deposition . 25

3.1.5 Design of experiments 25

3.1.6 Thermal and electron beam evaporation 26

3.2 Intrinsic layer characterization 27

3.2.1 Spectroscopic ellipsometry 27

3.2.2 Activation Energy and Dark conductivity 29

3.2.3 Raman Spectroscopy 31

3.2.4 Fourier Transform Infrared Spectroscopy (FTIR) 31

3.3 Characterization of solar cell performance 32

3.3.1 J-V curve measurement 32

4 Results **33**

4.1 Suitable conditions for intrinsic Germanium films 33

4.1.1 Effect of Temperature 33

4.1.2 Effect of GeH_4 flow on optoelectrical properties 36

4.1.3 Effect of Power and Pressure 40

4.1.4 Effect of Pressure 42

4.1.5 Effect of Power 44

4.2 a-Ge:H single junction device 46

4.2.1 Device architecture 47

4.2.2 Device stability 54

5 Conclusion and Recommendations **60**

5.1 Conclusion 60

5.2 Recommendations 61

List of Figures

2.1 The yellow region of the solar spectrum is AM0, and the red region is AM1.5 [23] 5

2.2 Doping process depicted using the bonding model [27] 8

2.3 Position of the Fermi level with change in doping concentration [27] 8

2.4 Germanium band structure with direct and indirect bandgap [32] 9

2.5 Illustration of three recombination mechanisms: Radiative recombination, Auger recombination and SRH recombination [35] 10

2.6 Thin film solar cell in superstrate configuration [46] 15

2.7 Energy band diagram of a p-i-n junction [47] 16

2.8 Spectral utilisation of a single junction vs multi junction solar cell [27] 17

2.9 Band diagram of a p-i-n/ p-i-n multi-junction solar cell representing tunnel recombination junction [48] 18

2.10 A solar cell's J-V curve depicting its MPP, corresponding J_{MPP} and V_{MPP}, as well as its J_{SC} and V_{OC} [48] 19

3.1 Illustration of PECVD, with its system compositions [51] 23

3.2 a) Thermal evaporation and b) E-beam evaporation 27

3.3 Energy band diagram of a p-i-n junction [51] 28

3.4 An example of activation energy calculation [65] 30

3.5 Fitted FTIR spectrum of a Ge:H film after oxidation [13] 32

4.1 Change in refractive index and deposition rate with substrate temperature . . 34
4.2 Change in absorption coefficient with substrate temperature 34
4.3 Intrinsicity of amorphous germanium with change in substrate temperature . 34
4.4 Material characteristics of the amorphous germanium samples with change in temperature 36
4.5 Change in activation energy with variation in germane flow 37
4.6 Change in band-gap with variation in germane flow 37
4.7 Change in refractive index with variation in germane flow 37
4.8 Intrinsicity of amorphous germanium with variation in germane flow 37
4.9 Changes in the deposition rate of the amorphous germanium with variation in germane flow 38
4.10 Material characteristics of the amorphous germanium samples with change in germane flow 40
4.11 Impact of the pressure and power on activation energy 41
4.12 Impact of the pressure and power on the bandgap 41
4.13 Impact of the pressure and power on the refractive index 41
4.14 Impact of the pressure and power on the deposition rate 41
4.15 Plasma at different pressures 42
4.16 Change in activation energy with variation in pressure 43
4.17 Change in band-gap with variation in pressure 43
4.18 Change in the refractive index with variation in pressure 43
4.19 Intrinsicity with variation in pressure 43

4.20 Change in activation energy with variation in power 44
4.21 Change in the bandgap with variation in power 44
4.22 Change in the refractive index with variation in power 44
4.23 Intrinsicity of the amorphous germanium with variation in power 44
4.24 FTIR characterization of the samples deposited at 3 mbar at varying powers . 46
4.25 J-V characteristics of the cell deposited in the p-i-n configuration 48
4.26 J-V characteristics of p-i-n configuration cells with varying thicknesses 49
4.27 Models of the first cell and the prospective cell configuration 50
4.28 J-V characteristics of the cell deposited in the p-i-n configuration with a ncSi p-layer 51
4.29 J-V characteristics of the cell deposited in the p-i-n configuration with a ncSi p-layer and buffer layer and hydrogen treatment 52
4.30 n-i-p configuration solar cell with varied doped p-layers 53
4.31 J-V characteristic of the p-doped solar cells 54
4.32 Stability measurement of the p-i-n configuration solar cell; top right : remeasured; bottom : Initial result 55
4.33 Stability measurement of the p-i-n configuration solar cell with 150 nm absorber 56
4.34 Raman spectroscopy of the germanium layer and solar cell deposited at 4.5 mbar and 12 W 57
4.35 Comparison of the samples deposited at 4.5 mbar and 12 W before and after exposure to ambient air 58

Nomenclature

Abbreviations

Abbreviation	Definition
PV	Photovoltaic
c-Si	Crystalline silicon
CdTe	Cadmium Telluride
CIGS	Copper Indium Gallium Selenide
nc-Si:H	Hydrogenated nanocrystalline silicon
eV	Electron Volts
PECVD	Plasma Enhanced Chemical Vapour Deposition
AM	Air Mass
UV	Ultraviolet
E_{ph}	Photon energy
E_V	Fermi energy
E_G	Band-gap energy
Ge	Germanium
GaInP	Gallium Indium Phosphide
InGaAs	Indium Gallium Arsenide
a-Ge:H	Hydrogenated amorphous germanium
SRH	Shockley-Read Hall
MHz	Megahertz
mbar	millibar
GeH_4	Germane
SiH_4	Silane
Si:H	Hydrogenated silicon

Abbreviation	Definition
RF	Radio frequency
ncSi:H	nanocrystalline silicon
SiO_x	Silicon oxide
CO_2	Carbon dioxide
PH_3	Phosphine
B_2H_6	Diborane
mm	milimeter
H_2	Hydrogen
TCO	Transparent Conductive Oxide
Al	Aluminium
Ag	Silver
Cr	Chromium
SE	Spectroscopic ellipsometry
E_{act}	Activation energy
E_g	Band-gap
σ_d	Dark conductivity
V	Voltage
σ_{ph}	Photo-conductivity
FTIR	Fourier Transform Infrared Spectroscopy
J_{SC}	Short circuit current
V_{OC}	Open circuit voltage
FF	Fill Factor
P_{max}	Maximum power
W	Watt
sccm	standard cubic centimeter per minute

1

Introduction

Solar power is the most plentiful energy source that can meet humanity's growing energy demands. The incident solar energy on the earth is estimated to be 10,000 times the electricity utilized by humans today [1]. Photovoltaic (PV) devices have been the holy grail of turning solar power into a secondary energy carrier, namely electricity. First-generation solar modules made of crystalline silicon (c-Si) are mass-produced and widely utilized [2]. One disadvantage of employing these modules is their thickness, which increases material costs and limits manufacturing to rigid modules. Furthermore, due to the supporting frame, these devices include a high concentration of glass and metal, which reduces the profitability of these modules [3].

Thin-film solar cells are the second generation of PV devices, and they are lightweight and can be made flexible. In this technique, the absorbing layer in the solar cell is generally 100 times thinner than in c-Si cells [4]. This enables for a significantly lower usage of material as the absorber layer [5]. Over time, the cost of creating these modules has decreased, resulting in cheaper modules. The efficiency of thin film solar technologies can also be high; III-V based thin film solar cells are the most efficient cells currently available, with a reported efficiency of 47.1% for a six-junction solar cell [6]. Additionally, there are other thin film

technologies such as Perovskites, CdTe, and CIGS that can easily surpass 20% [7], apart from amorphous silicon (a-Si) which has an efficiency of around 14% but the low efficiencies are counteracted by their low cost [8]. However, by monolithically adding several cells on top of each other, efficiency may be boosted to reach greater levels [9].

A multijunction solar cell is a device made up of many cells layered on top of one another. The different cells are intended to absorb various regions of the light spectrum, enhancing the total efficiency of the cell. Many ways have been investigated to build low-cost, high-efficiency devices to take advantage of the solar spectrum's area while avoiding thermalization losses. Perovskite-silicon tandem solar cells [10], and a-Si:H/nc-Si:H tandem solar cells [11] are some examples of these.

In all of these devices, the lower half of the solar spectrum with energy photons less than 1.1 eV is used in only certain cases, i.e, in III-V solar cells [12]. This lower part (high wavelength) of the solar spectrum is not utilized and is lost due to absorption losses due to lesser spectral utilization [13]. Creating a low bandgap absorber material that can access this portion of the spectrum might open the way for increased efficiency. The presence of a bottom cell allows using the part of the solar spectrum with higher wavelengths.

Germanium is a great contender for this purpose since it is a group IV element having a low bandgap. It is uncommon, but not exceptionally rare [14]. It possesses a direct bandgap of 0.8 eV and an indirect bandgap of 0.67 eV, making it perfect for use in the infrared part of the solar spectrum [15]. Crystalline germanium is known for its large charge carrier mobility, which has made it suitable for use in rapid-speed electronics [16]. As a result, extremely thin layers of Ge may be used as the absorber of solar cells, using little material. Thin films can be employed in devices having a p-i-n structure that contain amorphous or microcrystalline materials. Crystalline germanium has few defects, potentially leading to a better carrier transport, but it requires higher temperature processes for crystal growth. Amorphous germanium shows enhanced absorption coefficient at longer wavelengths in comparison to crystalline germanium, which is beneficial for solar cell applications [17]. According to [18]., amorphous germanium can be deposited at higher growth rates and lower temperatures, resulting in cost-effective and scalable solar cell production. Germanium amorphous has a higher defect density due to its disordered structure. These defects can

act as recombination centres that reduce solar cell efficiency [19]. To create Ge layers with low impurity concentrations, such a structure necessitates the introduction of hydrogen. In the non-crystalline structure, hydrogen passivates the dangling bonds. Hydrogenated germanium (Ge:H) may be manufactured cheaply utilizing a well-known commercial technology called Plasma Enhanced Chemical Vapour Deposition (PECVD).

1.1. Research objectives and outline

This study aims to develop a hydrogenated amorphous germanium absorber layer that may be employed as an intrinsic layer in a p-i-n structure device to produce germanium based high-efficiency thin-film devices. Previous research in the group resulted in films being prepared utilizing a counter-flow PECVD reactor [13]. It was discovered that oxidation had a significant impact on the characteristics of the material. This study employs a showerhead PECVD reactor, which can lead to improved control of reaction dynamics and films of desired material characteristics [20].

This work investigates the deposition of hydrogenated amorphous germanium by defining and assessing various deposition settings, and then applying these optimum parameters to create a single junction solar cell. To achieve this goal, the following three research questions were answered:

- What are the deposition parameters that affect the properties of the amorphous germanium?
- How do material characteristics influence the optoelectric properties of the germanium layers?
- What is the impact of the device architecture on the properties of the solar cell?

The report is arranged in the aforementioned manner. Chapter 2 provides background information regarding the photovoltaic effect, photovoltaic technologies, and various factors concerning the working of a solar cell. The processing and characterization approach is described in Chapter 3. The fourth chapter covers the results and examines their evaluations. Finally, Chapter 5 summarizes the results and provides recommendations for further research.

2

Background

2.1. Solar energy

Solar energy is essential to the operation of solar cells, which contribute greatly to sustainable energy solutions [21]. Sunshine that reaches Earth's atmosphere differs from that which reaches the Earth's surface. The strength of the solar spectrum is greatly influenced by the distance between Earth and the Sun, the angle at which the sun's rays enter the Earth's atmosphere, the weather, and the level of air pollution. AM 0 refers to the spectrum of the sun measured just outside the earth's atmosphere. The AM refers to the amount of air that the light has passed through before reaching the Earth's surface. AM 1.5 represents the spectrum irradiance, which is the incoming energy per square meter per second, as a function of wavelength [22].

The spectrum of the sun's electromagnetic radiation that reaches Earth spans ultraviolet to infrared, referred to as the AM1.5 solar spectrum. The spectrum comprises photons of distinct wavelengths, which determine its form and intensity. It can be expressed in terms of solar radiation or irradiance. Solar radiation refers to the direct emission of energy from the sun, whereas solar irradiance refers to the quantity of energy that reaches the surface of the Earth. The solar spectrum is displayed in Figure 2.1.

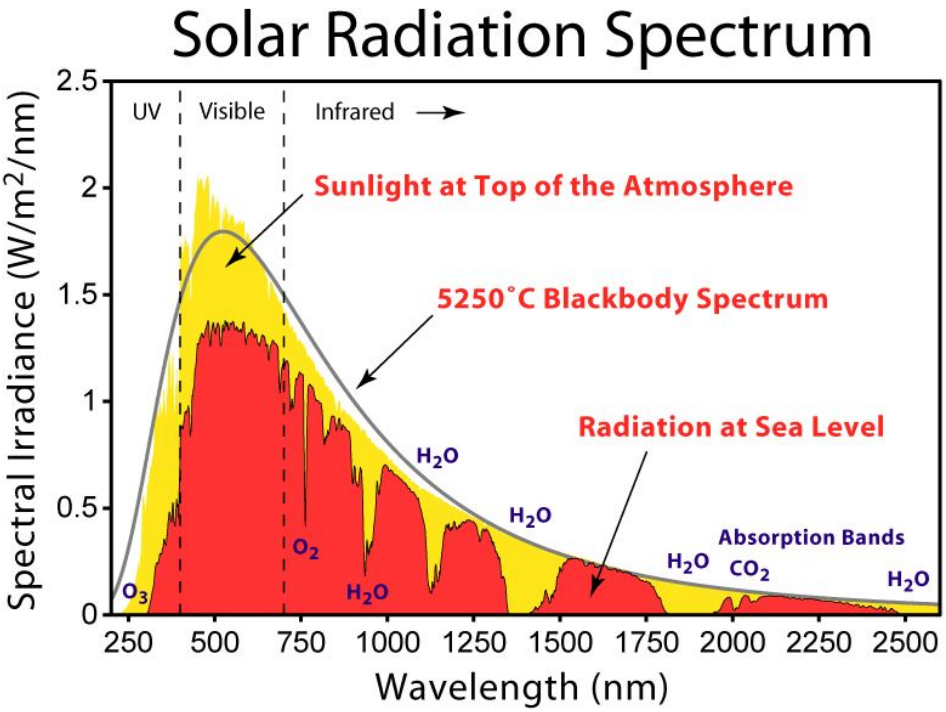


Figure 2.1: The yellow region of the solar spectrum is AM0, and the red region is AM1.5 [23]

Photovoltaic cells, which employ the photovoltaic effect for converting solar radiation into electricity, are highly sensitive to the shape and intensity of the sun's spectrum. The solar spectrum is separated into three major regions: ultraviolet, visible, and infrared. The UV refers to light having a wavelength less than 400 nm. The visible zone ranges from 400 to 700 nm. The infrared region spans from 700 nm to 2400 nm, This area comprises photons whose energy range from 0.5 to 1.8 eV [24].

The electromagnetic radiation is quantized and photons with different wavelengths have different energy according to:

$$E_{ph} = \frac{hc}{\lambda} \tag{2.1}$$

In this equation, photon energy in Joule is indicated by E_{ph}, h is Planck's constant, c is the speed of light in vacuum, and λ is the photon wavelength. As the wavelength increases, a photon's energy drops due to the denominator (λ). The solar spectrum contains a certain number of photons, which is different at each wavelength [25]. The spectral photon flux, or

the quantity of photons per unit area per second as a function of wavelength, is given by:

$$\phi(\lambda) = P(\lambda)\frac{\lambda}{hc} \tag{2.2}$$

$\phi(\lambda)$ is the spectral photon flux in photons $m^{-2}\ nm^{-1}$, whereas $P(\lambda)$ is the spectral power per wavelength. The spectral photon flux holds significance, as the current generated by solar cells is directly proportional to the quantity and energy of photons emitted on them.

2.2. Semiconductor properties

Within an isolated atom, electrons can only occupy discrete energy levels. In semiconductors, its atomic structure creates a range of acceptable energy levels for electrons, called energy bands, as well as ranges of prohibited energy states, called forbidden gaps or band gaps. The mobility of electrons that have been liberated from their bonds with atoms is what allows charge to be transported in semiconductors. Therefore, our attention is directed towards the energy levels that correspond to valence electrons. Valence electrons, which form covalent bonds, have permissible energies within the valence band (VB). When these electrons are released from their covalent bonds, they enter the conduction band (CB), which includes the permissible energy levels for free electrons. A band of prohibited energy levels separates the valence and conduction bands. The maximum possible energy inside the valence band is written by E_V, whereas the lowest probable energy of the conduction band is marked by E_C. The energy difference between the borders of these two bands is known as the band gap energy, or simply the band gap (E_G). This is an important property of the material.

$$E_G = E_C - E_V \tag{2.3}$$

The operation of every semiconductor device is fundamentally dependent on the quantity of charge carriers that transport charge within the semiconductor, resulting in electric currents. To precisely evaluate and appreciate how these devices work, it is critical to know the precise concentration of these charge carriers. A material is known to be in thermal equilibrium when there is no external energy input and recombination and generation rates even out.

The Fermi-Dirac distribution describes the probability that a specific energy state is occupied by holes or electrons in thermal equilibrium. The Fermi energy, also called Fermi level (E_F) is the electrochemical potential of the electrons in a material and in this way it represents the averaged energy of electrons in the material. The position of the Fermi level in relation to the band energy levels is critical in influencing a material's electrical characteristics [26].

In an intrinsic material, every released electron leaves a hole, and every hole that annihilates takes an electron with it. This produces identical concentrations of electrons (n) and holes (p). These amounts can be adjusted by doping. Doping can be implemented by including atoms of different elements to substitute semiconductor atoms in the crystal lattice. In a silicon lattice, silicon atoms can be swapped by either boron or phosphorous atoms. Because silicon contains four valence electrons, it may form four covalent bonds. Boron and phosphorus contain three and five valence electrons, respectively. When a silicon atom is replaced by a phosphorous atom, four out of five valence electrons are used to form bonds with the surrounding silicon. Thermal energy is generally used to boost phosphorous' fifth valence electron because there are no other valence electrons available. Similarly, boron can only bond to three germanium atoms, creating a hole in the lattice. Phosphorous contributes an additional electron to the lattice, whereas boron can get an electron through a Si-Si connection. These dopants are hence known as electron donors and acceptors, respectively. n-type materials are semiconductors that have been doped with electron donors. On the contrary, doping intrinsic material with electron acceptors produces p-type material. The dopants have no effect on the bulk's net charge, since the charge of the nucleus is the same as that of its electrons. The dopant atoms ionize when they give or take an electron out of the lattice, as illustrated in Figure 2.2.

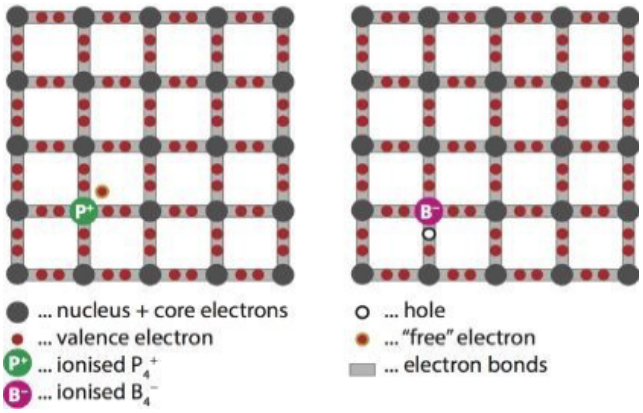


Figure 2.2: Doping process depicted using the bonding model [27]

Doping also impacts the Fermi energy's level. When the electron concentration is raised by raising the donor concentration, the Fermi energy rises, which is shown by moving the Fermi energy near the conduction band on the band diagram. In p-type materials, the Fermi energy is closer to the valence band. Figure 2.3 shows the variations in Fermi energy levels.

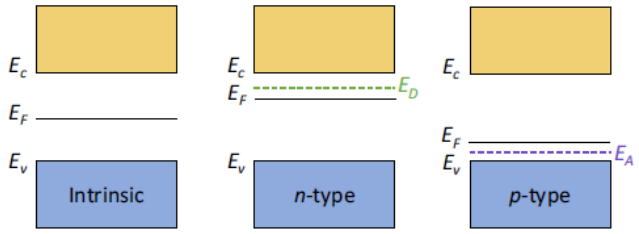


Figure 2.3: Position of the Fermi level with change in doping concentration [27]

2.2.1. Germanium properties

Germanium is a semiconductor material commonly used in microelectronics and sometimes in III-V solar cell technologies [28]. In its crystalline form, it has a structure similar to that of other group IV elements, with four valence electrons forming covalent bonds with neighbouring atoms. It can have an amorphous structure, just like silicon. One of the primary characteristics of germanium as a semiconductor material is its diminutive bandgap of approximately 0.67 eV in its crystalline form. This bandgap is indirect. Crystalline germanium has a direct bandgap state of 0.8 eV [29]. Both the bandgaps can be seen in the band structure (Figure 2.4), showing the energy levels with the wave vector. A wave vector is a mathematical quantity that characterizes the momentum of a particle, such as

an electron, in the crystal lattice of the material. It is often represented by the symbol 'k'. This implies that the maximum energy point of the conduction band and the minimum energy point of the valence band occur at different momentum values in the reciprocal lattice. In other words, the electron transitions between the valence band and the conduction band involve a change in momentum, rendering the process less probable in comparison to materials with direct bandgaps. Germanium's narrow bandgap leads to a low open circuit voltage, high rate of recombination of electron-hole pairs, reducing overall efficiency [30]. This makes germanium less efficient than silicon for some applications. Despite being both indirect bandgap materials, germanium generally exhibits a higher absorption coefficient than silicon in the visible and near-infrared regions [31].

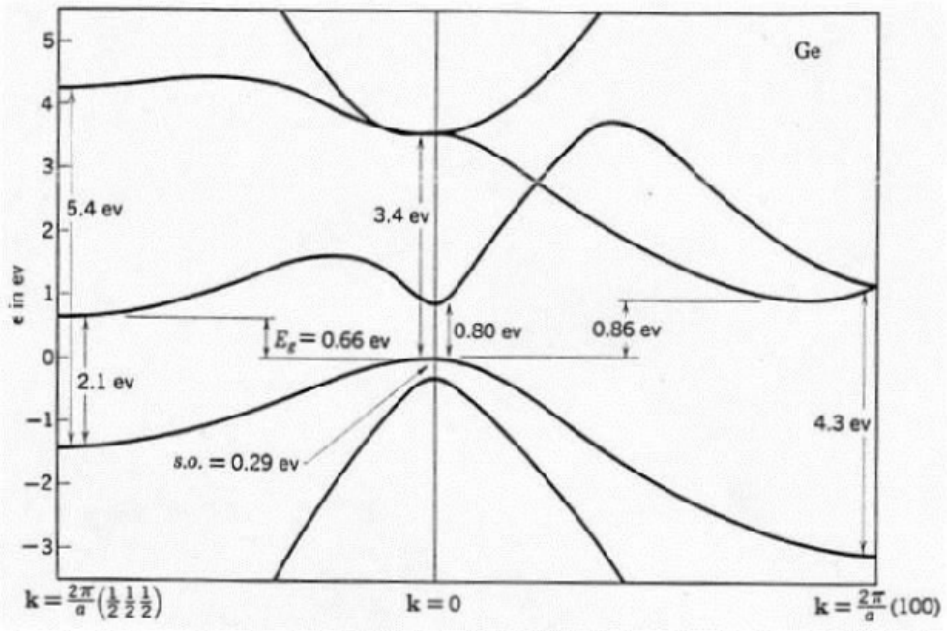


Figure 2.4: Germanium band structure with direct and indirect bandgap [32]

Germanium has, thus, become a good choice for applications requiring high-speed electronics, such as in some transistors [16]. These properties also make germanium an ideal candidate as a bottom cell for PV applications. Crystalline germanium has been used in high-efficiency multijunction solar cells where Ge is used as the substrate [6]. However, the use of germanium as a low-bandgap material for solar cells is limited by its high cost and difficulty in growing high-quality germanium crystals. Therefore, germanium is typically used only in high-efficiency, niche applications, such as in space-based solar panels,

where its superior performance justifies the higher cost [10]. The best configuration cell using GaInP/InGaAs/Ge structure has obtained an efficiency of 31.7% under one sun AM0 illumination [33]. A study on amorphous germanium nanoabsorber solar cells estimated that an optimized (hydrogenated amorphous germanium) a-Ge:H solar cell with an only 25 nm thick absorber layer can achieve a single cell efficiency of about 5% [15].

2.3. Recombination mechanisms and losses

Solar cell functioning involves three steps: generation, separation, and collection. When light penetrates a medium, it is (partially) absorbed as it travels through it. If the photon energy exceeds the semiconductor's bandgap energy, it is sufficient to break bonds and excite a valence electron into the conduction band, leaving a hole in the valance band. Thus, electron-hole pairs are formed. The process is referred to as photogeneration. The acquired energy can be gathered if both particles separate, and then permitted to recombine after having traversing an electric circuit. If recombination takes place elsewhere, the energy is wasted [34]. Three separate recombination processes are identified: Radiative, Shockley-Read-Hall, and Auger. Furthermore, thermalization is a non-recombination loss mechanism that should be taken into account. The three recombination techniques are illustrated in Figure 2.5.

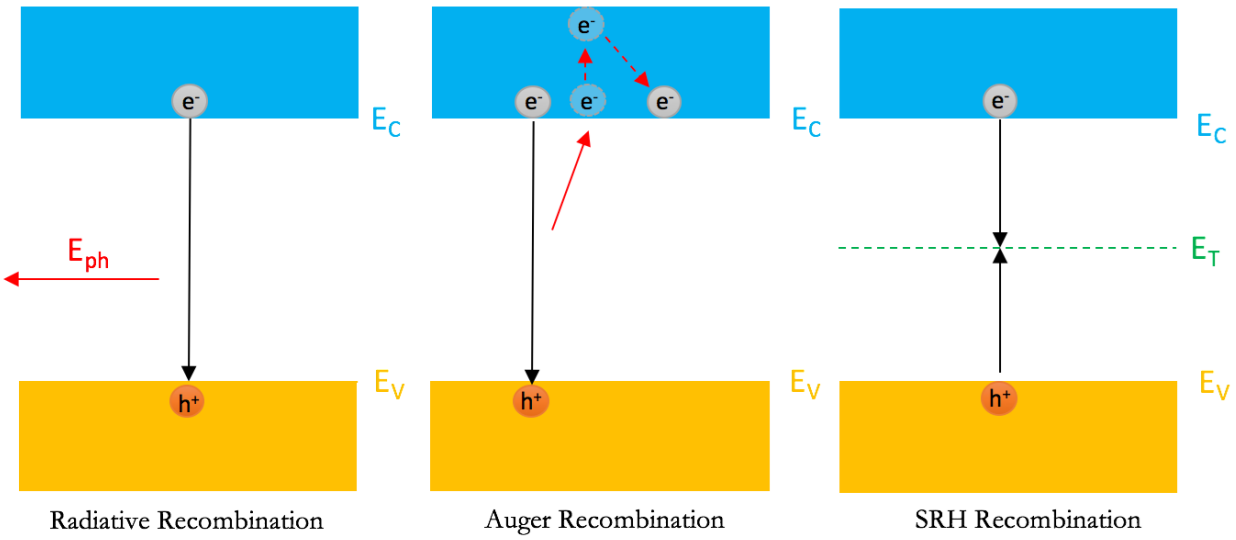


Figure 2.5: Illustration of three recombination mechanisms: Radiative recombination, Auger recombination and SRH recombination [35]

Radiative recombination, also known as direct recombination, occurs when an excited electron contacts a hole in the valence band. The difference in energy between the two states, known as the bandgap energy, is released when a photon of that wavelength is emitted. Radiative recombination is more noticeable in direct bandgap materials like gallium arsenide than in indirect bandgap materials like crystalline silicon and crystalline germanium. For materials with an indirect band gap, the top end of the valence band and the bottom end of the conduction band are offset in terms of momentum, necessitating an additional phonon interaction. This extra requirement reduces absorption in the material while simultaneously suppressing radiative recombination [34].

Shockley-Read-Hall (SRH) recombination is often referred to as trap-assisted recombination. This sort of recombination is found within indirect bandgap materials due to trap densities. Since charge carriers tend to make smaller energy leaps, trap states located midway between band boundaries have the highest recombination rate because they combine the smallest energy differences. Doped layers are required for solar cell performance. However, they have a high defect density and rate of SRH recombination. SRH recombination in bulk materials can be reduced by ensuring excellent material quality and few defects. The surface recombination caused by the lack of neighbouring atoms can be reduced by passivating the dangling bonds with hydrogen. Because of its single valence electron, hydrogen effectively passivates germanium dangling bonds, resulting in reducing the dangling bonds when it binds to germanium [35].

Auger recombination is a three-particle recombination mechanism. An electron and a hole recombine, but instead of dissipating the energy in the form of heat or a photon, a third particle takes it and stimulates it further into the conduction or valence band for electrons or hole [36]. The excited particles relax to the band edge, transferring their momentum and energy to the lattice, which then emits heat. The significance of Auger recombination increases when multiple charge carriers are combining and absorbing and dissipating energy during recombination. High charge carrier concentrations are achieved by high doping concentrations or concentrated solar photovoltaic technology, which concentrates light into a narrow region.

Thermalization is a non-recombination loss process. When electrons absorb photons with

$E > E_g$, they are excited far into the conduction band or, in the case of holes, deeper into the valence band. In a relatively short period, the extra energy will be thermalized, causing the energy state to relax to the lowest energy state in the conduction band and highest energy state in the valence band via phonon emission. Although all the energy of photons is absorbed, only the bandgap energy may be employed to generate electricity.

2.4. Photovoltaic technologies

Several approaches have been developed to build solar cell devices, each utilizing a different semiconductor material and production method. Here are some noteworthy examples:

- **Micromorph cells**: Micromorph solar cells combine amorphous and microcrystalline silicon layers to improve solar energy conversion efficiency. The name micromorph refers to the cells' structure, which is composed of thin layers of both amorphous and microcrystalline silicon layered on top of one another. The micromorph design utilizes the complimentary characteristics of a-Si and μc-Si. Amorphous silicon absorbs higher-energy photons more effectively than microcrystalline silicon, which is better suited to absorbing lower-energy photons. By stacking both these layers, a greater section of the solar spectrum may be absorbed, boosting the total efficiency of the solar cell. Micromorph solar cells can display efficiency of up to 14% [37].
- **Group III-V solar cells**: This technique employs compound semiconductors from the III-V group of the periodic table, including gallium indium phosphide (GaInP), gallium indium arsenide (GaInAs), and gallium arsenide (GaAs). These materials have exceptional optoelectronic capabilities and can absorb various wavelengths of the sun's spectrum. By carefully controlling the layer thickness as well as bandgap energies, III-V compound semiconductor tandem cells can attain record-breaking efficiencies. For example, in 2022, a Fraunhofer ISE research team set a new efficiency benchmark of 47.6% for a quadruple junction solar cell with 665 sun illumination [38]. III-V technology has additionally been coupled with Germanium to create highly efficient multijunction devices [39]. This cell employs GaInP/GaInAs/Ge subcells to produce a device with a 41.1% efficiency under focused irradiation of 454 suns. This efficiency is achieved by current matching and the use of buffer layers to counteract

lattice mismatching between various materials.

2.4.1. Generation of solar cells

Solar cells have evolved over time, with each generation bringing its own set of benefits and drawbacks.

First-generation solar cells, based on silicon wafers, are the most mature and commonly used photovoltaic technology. These cells are constructed from either monocrystalline or polycrystalline silicon, which is recognized for its excellent efficiency and long-term durability. Monocrystalline silicon cells are cut from a single crystal and are more efficient but more expensive to manufacture than polycrystalline cells, which are formed from several silicon crystals. Due to their proven performance and cost-effectiveness, first-generation cells dominate the market. However, they take many raw materials and energy to produce, which might influence their total environmental footprint [40].

Second-generation solar cells, commonly known as thin-film solar cells, use a range of materials, such as amorphous silicon, cadmium telluride (CdTe), and copper indium gallium selenide (CIGS). The lightweight and adaptable nature of these cells renders them suitable for a diverse range of applications, including integrated photovoltaics and mobile solar equipment. Thin-film technologies often require fewer material and energy to manufacture than first-generation cells, resulting in reduced manufacturing costs [41].

Third-generation solar cells are new technologies that attempt to improve efficiency beyond existing silicon-based cells. These consist of organic photovoltaics, perovskite solar cells, dye-sensitized solar cells, and quantum dot solar cells. These technologies frequently use innovative materials and architectures to increase light absorption and efficiency. For example, perovskite solar cells have shown rapid efficiency gains and are regarded as extremely promising given their low cost of production and adaptability. Nonetheless, numerous third-generation technologies are still in the research and development stage, and they encounter challenges related to stability, scalability, and environmental concerns [42].

Fourth-generation solar cells commonly referred to as hybrid inorganic cells or nano-photovoltaics, represent the most recent innovation in photovoltaic technology. They com-

bine the cheap cost and flexibility of polymer thin films with the durability of organic nanostructures, such as metal nanoparticles, oxides, carbon nanotubes, graphene, and their derivatives [43]. Current research aims to produce low-cost manufacturing procedures that preserve high efficiency [44].

2.5. Single junction solar cell

For decades, single junction solar cells have been the foundation of photovoltaic technology, converting sunlight into power with a simple junction. These cells, normally manufactured from crystalline silicon, display a theoretical efficiency limit called as the Shockley-Queisser limit, that is roughly 33.7% for a single p-n junction in regular terrestrial sunlight [45]. However, when working with amorphous semiconductors, which have distinct characteristics and problems than crystalline materials, alternate structure of cells are frequently used. The p-i-n configuration is widely used, as amorphous semiconductors with many traps or defects are benefited by the intrinsic layer, which provides a region with fewer defects for charge transport. This design includes an intrinsic layer in between the p- and n-type regions, which is the main absorber layer of the cell. The intrinsic layer improves photon absorption, leading to higher quantum efficiency. However, the choice between p-i-n and p-n structures ultimately depends on factors such as the specific material properties.

2.5.1. p-i-n junction

The separation of photo-generated pairs of electrons and holes is crucial for the performance of solar cells, as it prevents recombination.

p-layer: The p-layer, is composed of a semiconductor material wherein boron, as it has one less valence electron, creates places where there is a lack of charge.

i-layer: The i-layer, also known as the intrinsic layer, which is the absorber layer in this cell is formed of an undoped or weakly doped semiconductor material. It is also where the main electric field needs to be created for the separation and collection of photo-generated charge carriers. When sunlight reaches the i-layer, it creates electron-hole pairs.

n-layer: The n-layer, is composed of a semiconductor material with a surplus of electrons.

Doping the silicon layer with impurities like phosphorus provides “free” electrons in the semiconductor’s conduction band.

Sunlight enters the solar cell as photons. Photons land on a thin and transparent p-layer known as the window layer, known as the window layer. After passing through the window layer, photons reach the intrinsic layer and are absorbed. Photons are absorbed in the thick intrinsic layer, with the surplus entering the n-layer and being reabsorbed in the n layer. The absorption depends on the reflection at the interfaces before the absorber layer, light trapping and bandgap of the different layers, especially the absorber layer. A schematic of the p-i-n (superstrate) configuration is shown in Figure 2.6. Absorbing photons excite electrons and create holes in the valence band.

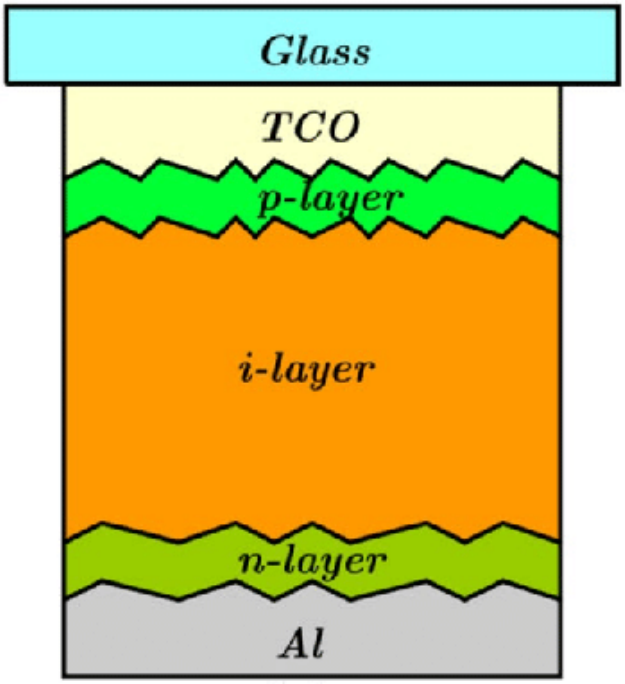


Figure 2.6: Thin film solar cell in superstrate configuration [46]

Photons are largely absorbed in the intrinsic layer, resulting in electron-hole pairs. The intrinsic layer is intended to be the primary light-absorbing zone. The p- and n-doped areas form an electric field across the intrinsic layer, which separates the generated electrons and holes. Electrons are drawn to the n-type area, and holes to the p-type zone. In the depletion zone, the drift electric field drives electrons and holes to their corresponding n-doped and p-doped areas. This produces the generated photo-current. In the quasi-neutral

regions (p and n layers), carriers travel by diffusion. The scattering electric field propels holes towards the p-doped area and electrons toward the n-doped region. This leads to the scattering photo-current. The total photo-current is the generation and scattering currents. Boron atoms with extra electrons are negatively charged, whereas phosphorous atoms are positively charged. This creates an electric field across the intrinsic bulk if the intrinsic layer is thin and the concentration of dopant is high enough.

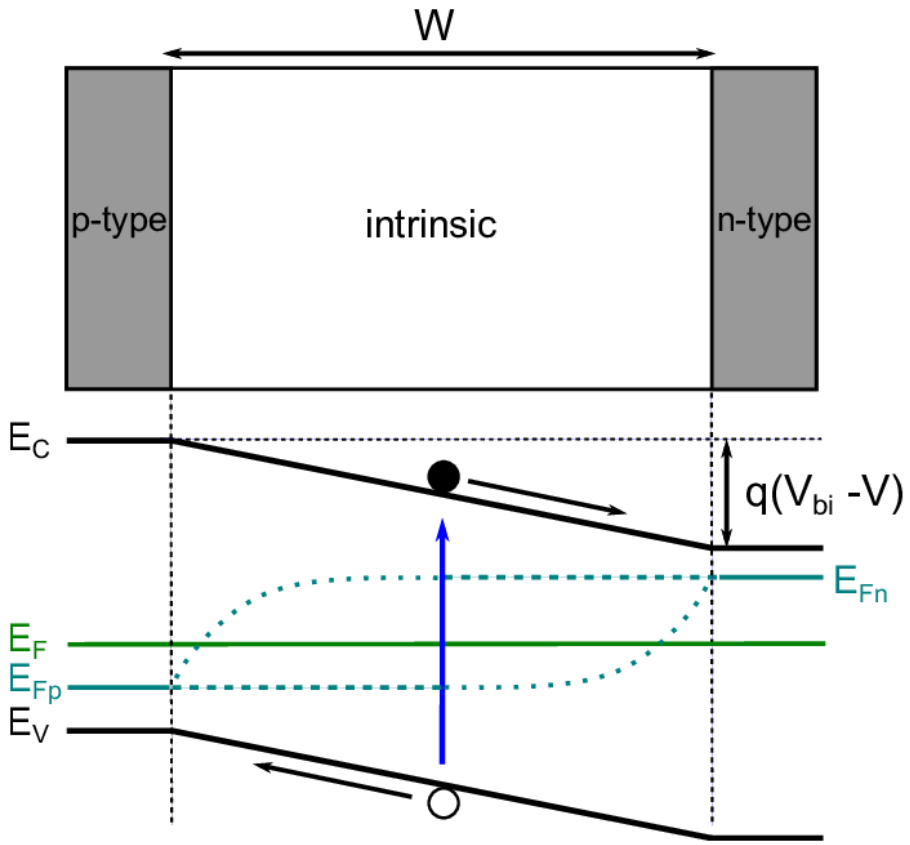


Figure 2.7: Energy band diagram of a p-i-n junction [47]

2.6. Multi-junction solar cell devices

Thin-film solar cells using a multi-junction configuration have the capacity to achieve both extremely high efficiency and relatively low costs. The core idea underlying these solar cells is the use of numerous p-n or p-i-n junctions, each constructed from a different semiconductor material. Multi-junction cells combine materials with distinct bandgaps to convert sunlight into energy, as depicted in Figure 2.8. To achieve this, multiple cells are

stacked on top of each other. The top cell has the greatest bandgap and can absorb and convert short-wavelength/blue light. Light with longer wavelengths than the bandgap wavelength can pass through the top cell and be absorbed by cells with smaller bandgaps below. The bottom cell has the lowest bandgap and absorbs long-wavelength/red and near-infrared light. To maximize the performance of multi-junction solar cells having two electrical terminals, the currents of all subcells must be matched.

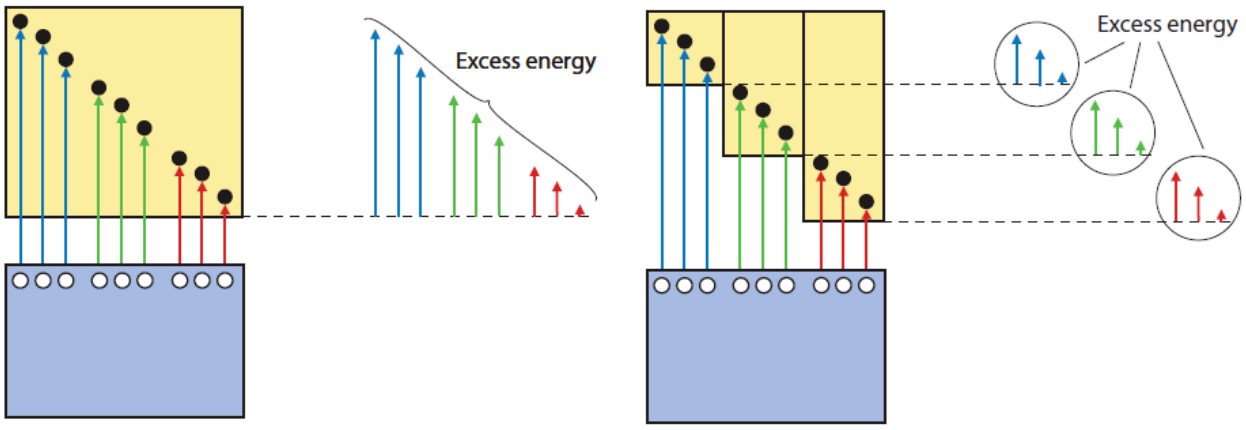


Figure 2.8: Spectral utilisation of a single junction vs multi junction solar cell [27]

Multi-junction solar cells act similarly to single-junction solar cells that are electrically coupled in series. The electrical potentials pile up, but the current passing through subcells is equal and restricted by the solar cell that produces the least amount of current. The functioning of a multi-junction solar cell will be illustrated by a p-i-n/p-i-n structure. The electron-hole pairs formed by each junction's intrinsic absorber layer are separated by internal electric fields generated by the subcells' p and n layers. The front contact collects holes created in the top cell, while the rear contact collects electrons generated in the lower cell. In a double junction, or a tandem device, electrons from the top cell are directed towards the top cell's n-layer, while holes created in the bottom cell are directed towards the bottom cell's p-layer, which is next to the top cell's n-layer. Figure 2.9 shows the band diagram of the described multi-junction solar cell. While a p-i-n/p-i-n structure is depicted and described, multi-junctions can also have a p-i-n/p-n configuration. Although recombination is undesirable in the bulk of the solar cells, it is required in the tunnelling recombination junction, where the two subcells are connected. A lack of recombination at this p-n interface

might lead to the build-up of charge carriers, which might degrade the electric field across the intrinsic absorber layer, limiting the collection of photo-generated charge carriers.

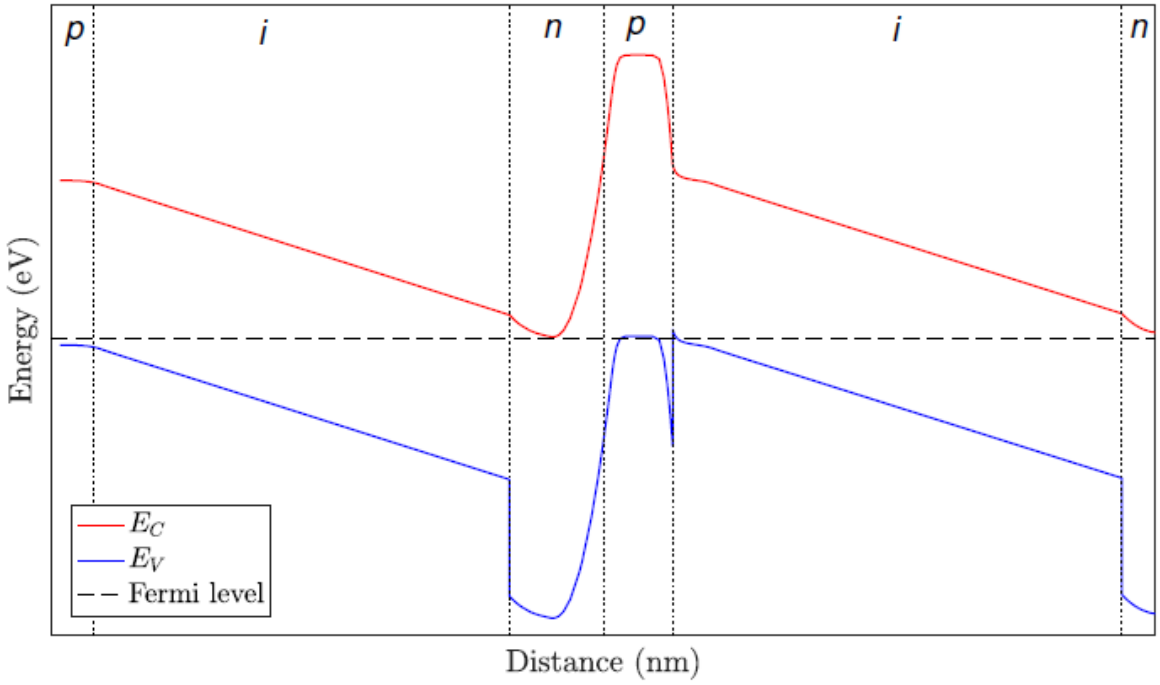


Figure 2.9: Band diagram of a p-i-n/ p-i-n multi-junction solar cell representing tunnel recombination junction [48]

2.6.1. Solar cell performance

Four metrics are used to assess solar cell performance. The efficiency η, the short circuit current density J_{SC}, the open circuit voltage V_{OC}, and the fill factor (FF).

The open circuit voltage V_{OC} represents the separation and accumulation of charge carriers at the contacts. The amount of charge that may be collected is restricted by mutual repulsion and carrier lifetimes. J_{ph} is the photo-generated current density and J_0 is the saturation current density. J_0, referred to as the recombination parameter, is a complex number that should be maintained as low as feasible [49].

$$V_{OC} = \frac{nk_BT}{q} ln(\frac{J_{ph}}{J_0}) \tag{2.4}$$

The thermal voltage is defined as the product $k_B.T.q^{-1}$, which includes the Boltzmann

constant (k_B), temperature (T), and elementary charge (q). The voltage at 300 K is around 0.0259 V, which is a fundamental parameter for semiconductors. The diode ideality factor, n, equates to one for an ideal diode and can range up to three depending on the device's principal recombination process [50].

J_{MPP} and V_{MPP} are the related values of current density and voltage at the maximum power point (MPP) and their product is the maximum produced power density, P_{max}. The fill factor (FF) indicates how effectively the solar cell maintains its J_{SC} and V_{OC} up to the maximum power point. The FF is a ratio of a solar cell's maximum power to its potential maximum power.

$$FF = \frac{J_{mpp} V_{mpp}}{J_{SC} V_{OC}} \tag{2.5}$$

Figure 2.10 illustrates that the FF is the ratio of the surface area of squares created by Pmax multiplied by JSC and VOC.

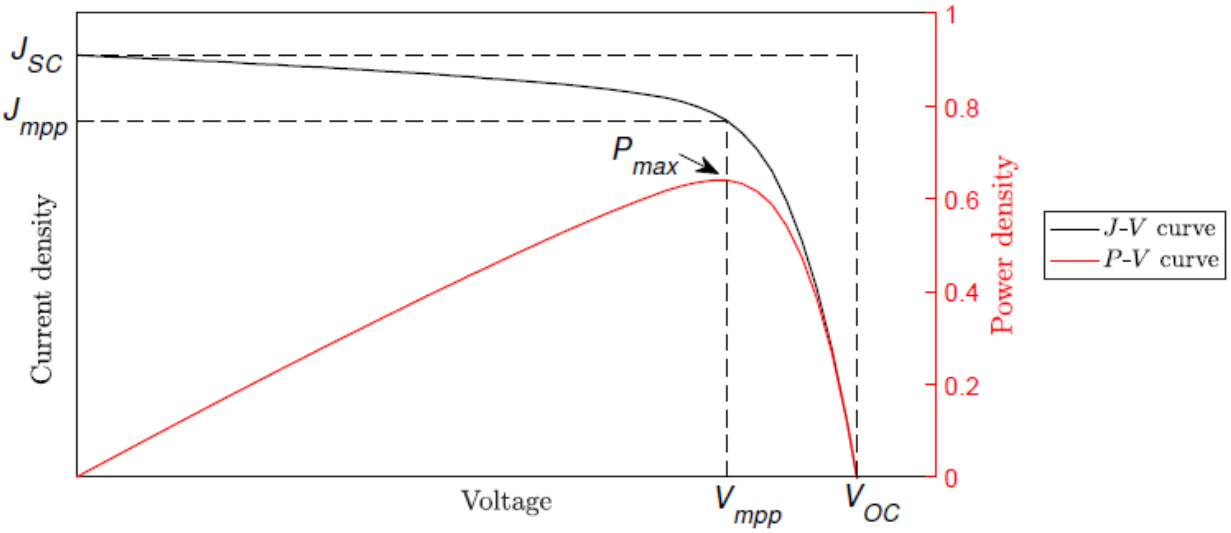


Figure 2.10: A solar cell's J-V curve depicting its MPP, corresponding J_{MPP} and V_{MPP}, as well as its J_{SC} and V_{OC} [48]

When the power generated is determined, the conversion efficiency may be computed by utilizing the power incident upon the cell's surface per unit area, P_{in}, utilizing

$$\eta = \frac{P_{max}}{P_{in}} = \frac{J_{mpp}V_{mpp}}{P_{in}} = \frac{J_{SC}V_{OC}FF}{P_{in}} \tag{2.6}$$

3

Methodology

3.1. Processing techniques and equipment

3.1.1. Substrate preparation

The substrates are first cleaned in an ultrasonic acetone bath for 10 minutes, then dried using compressed nitrogen before being cleaned again in an ultrasonic isopropylalcohol bath for 10 minutes. The substrates are dried with compressed nitrogen once again. The substrates in this case being the 2.5 cm x 10 cm 1.1 mm thick corning glass which are used to deposit the germanium layers and the textured ASAHI VU which already has a SnO_2:F TCO. The substrate is then loaded on a holder containing a mask which leaves enough space at the top and bottom edges for the front contacts to be exposed.

As FTIR characterization is also performed on the germanium layers, a quarter of a crystalline wafer of the 100 orientation is also placed in the substrate holder for the layers to be deposited on it.

3.1.2. Plasma Enhanced Chemical Vapour Deposition (PECVD)

Plasma Enhanced Chemical Vapour Deposition (PECVD) is a thin-film deposition process using plasma to accelerate the chemical interaction between gases and substrate material, resulting in the formation of a thin layer on the substrate's surface. PECVD is widely employed in semiconductors to deposit thin films of a variety of materials, including silicon dioxide, silicon nitride, and amorphous silicon.

The p, i, and n layers are formed using PECVD. PECVD is a deposition process that employs a plasma as shown in Figure 3.1 to deliver energy to numerous precursor gases in a low pressure chamber, causing them to dissociate and adsorb to a neighboring substrate. An alternating current of 13.56 MHz is applied to an electrode whilst the substrate holder remains grounded. Following plasma ignition, electrons are accelerated by the electric field produced between the powered and grounded electrodes, causing them to collide with the precursor gases, which are then dissociated, resulting in ionised radicals. Because the grounded electrode has a lower potential than the RF electrode, positively charged radicals and neutral particles only reach the substrate and are adsorbed, forming layers on it. Layer materials and attributes may be changed by adjusting the precursor gases, their flow rates, and hence their relative composition, RF power density, and ambient pressure and temperature.

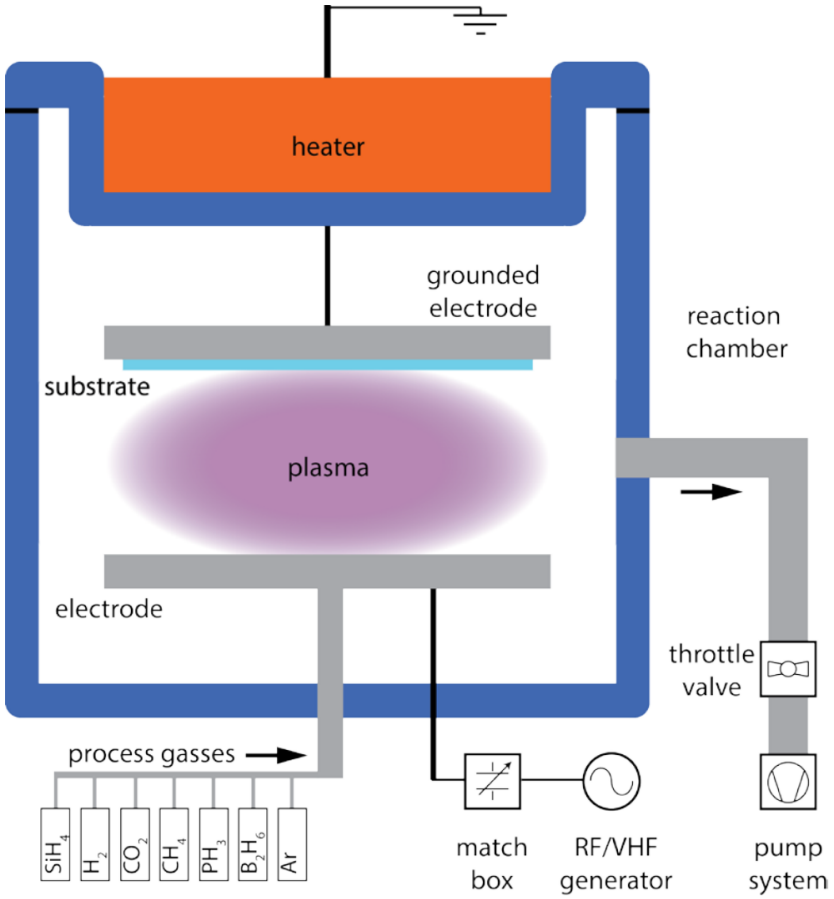


Figure 3.1: Illustration of PECVD, with its system compositions [51]

The equipment used in this thesis is an Elettrorava PECVD multichamber tool known as AMIGO. Substrates are put inside a load lock chamber, which allows air to be evacuated. When the chamber achieves a pressure of around 15-25 mbar, the substrate of choice is transferred to one of six additional heated vacuum chambers containing the electrodes and gas inlets and outlets. Various chambers have various gas inlets and are conditioned with unique materials to reduce cross contamination. Germane (GeH_4) and hydrogen (H_2) is used to deposit hydrogenated amorphous germanium (a-Ge:H). Silane (SiH_4) and hydrogen gas are utilized to form hydrogenated silicon layers (Si:H), with additional factors such as RF power, pressure, and temperature governing the formation of amorphous (a-Si:H) or nanocrystalline structures (nc-Si:H). Hydrogen passivates any dangling bonds that persist after nucleation. Silicon oxides (SiO_x) are produced by combining silane with carbon dioxide

(CO_2). Phosphine (PH_3) and diborane (B_2H_6) serve as n- and p-dopants, respectively.

3.1.3. Germanium intrinsic layer deposition

This section explains the processes taken for depositing the intrinsic germanium layer. Important aspects of the PECVD technique that might effect materials are discussed. This is followed by past study findings explaining the many conditions that might result in an excellent film. Finally, the design of experiments used in this study is discussed.

For the majority of measurements, germanium thin films have been deposited on 1.1 mm thick corning gorilla glass, with the exception of (100) silicon wafers used for FTIR measurement (see subsection 3.2.4). There are seven major characteristics that can influence material properties:

- Germane (GeH_4) flow: This is the germanium precursor gas which dissociates when introduced into plasma. Germanium atoms then mix to create a layer upon the glass substrate. In other situations, the gas may not entirely dissociate, resulting in radicals like GeH_3, which are also part of the layer.
- Hydrogen (H_2) flow: In addition to hydrogen derived from GeH_4, hydrogen flow aids in the passivation of dangling germanium bonds creating the Ge:H alloy.
- RF Power: This refers to the power sent to the plasma via the electrodes.
- Pressure: This refers to the pressure within the chamber wherein the deposition occurs.
- Deposition Time: This is how long the plasma remains on. During this period, deposition occurs, which may change the material's thickness.
- Temperature: This is the substrate's temperature.
- Electrode Distance: The distance between the two electrodes in the deposition chamber. This parameter affects capacitance, resulting in variations in the strength of the electric field.

3.1.4. Previous research and obtaining optimum conditions for deposition

Literature shows that hydrogenated germanium has previously been deposited using a variety of production processes, including RF [52], DC magnetron sputtering [53], thermal evaporation [54], and glow discharge chemical vapour deposition [55]. One aspect of interest for these films was their density [52]. However, the densest films created were extremely thick (40 μm) for thin-film PV applications since the defect density would restrict the output current. The second study found that introducing oxygen in the samples reduced their activation energy, making them more n-type [53]. Finally, temperature is identified as a crucial factor [54], [55]. It is revealed that substrate temperature affects the crystalline quality of the deposited films. Amorphous films are created at low substrate temperatures (about 200°C) [56], while high temperatures (approximately 400-500°C) yield highly crystalline films. Some research has also been conducted on the RF PECVD processing of thin film germanium [57] [13]. This study also supports the hypothesis that temperature influences material qualities such as crystallinity and density. Furthermore, when the electrode spacing grows, the material's photoelectronic characteristics deteriorate.

3.1.5. Design of experiments

Previous studies conducted in the PVMD research group [13] provided information on the starting temperature and electrode distance. It has been shown that a narrower electrode spacing improves the processing of denser films, characterized by a greater refractive index, lower E_{04}, and higher E_{act}. The samples deposited at higher temperatures of 275 °C have a high refractive index [58]. Four of the seven factors indicated in section 3.1.2 that impact film properties—temperature ranging from 82 °C to 275 °C, RF power ranging from 12 to 25 W, pressure from 2 - 6 mbar, and Germane flow from 1 to 5 sccm at intervals of 1—are modified in this study. Electrode distance was not varied as a small gap produced best results as mentioned above. The deposition time was kept constant at 500 seconds as previous research found that the samples deposited in this much time were of a thickness that are representative of the films to be used in the solar cell [58]. Hydrogen was kept at 200 sccm which is the maximum flow rate achievable as a higher hydrogen flow rate passivates the dangling bonds leading to better quality films [13], [58].

It must be noted that previous studies in the group [13] utilized a PECVD reactor with background gas injection. This study used a showerhead PECVD arrangement rather than background gas injection. The showerhead is generally made up of a gas distribution plate facing the substrate and an electrode. The gas distribution plate has a series of regularly spaced gas holes or nozzles via which process gases are supplied into the reaction chamber. These holes are intentionally placed to facilitate even gas flow and dispersion over the substrate surface. A homogenous plasma production should result in constant and regulated film deposition on the substrate.

3.1.6. Thermal and electron beam evaporation

Before and after the solar cell layers are deposited, the front and back metal contacts get evaporated onto the substrate. This process is also used to deposit front contacts for the germanium layers to measure activation energy, dark and photo-conductivity. Thermal and electron beam evaporation are utilized, both of which involve evaporating a metal at low pressure. When the gaseous metal particles come into touch with the interior of the chamber, they solidify. The low pressure guarantees that the metal vapor is evenly distributed throughout the chamber. To create patterns on the cells and germanium layers for carrying out measurements, samples are put in a holder having a shadow mask, facing the evaporating metal, and spun at a low speed (around 20 rpm). E-beam evaporation is a method for evaporating a target material utilizing a high intensity electron beam directed at a target material within a crucible by a magnetic field. Thermal evaporation employs a tungsten evaporation boat to hold the bulk metal. A strong current flows through the evaporation boat, which warms up by dissipating a portion of the current because of its electrical resistance. One technique of evaporation may be preferred over another due to its high melting point (Cr), alloying behavior with the tungsten boat (Al), or the emission of possibly dangerous UV radiation due to the high intensity e-beam (Al). Both evaporation procedures are accessible in the PROVAC machine, which is present in the EKL laboratory at TU Delft and is shown in Figure 3.2.

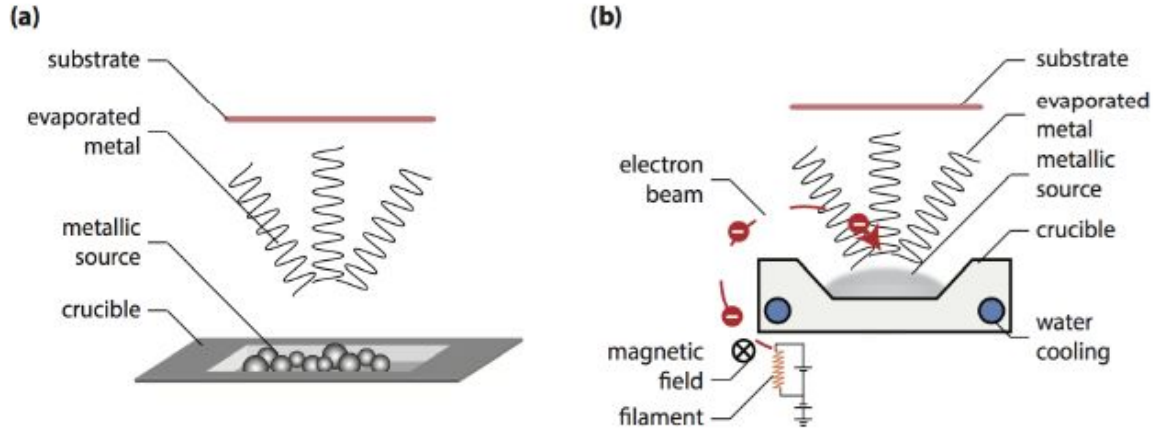


Figure 3.2: a) Thermal evaporation and b) E-beam evaporation

500 nm Al is utilized to gather charge carriers carried by the TCO for the solar cell's front contacts ,as well as the conductivity measurements on germanium layers. A mask is utilized, to achieve the desired patterns. The rear contact of the solar cell is made of an Ag/Cr/Al stack having thicknesses of 500, 30 and 800 nm, respectively. The Ag layer is thermally vaporized, serving as a back reflector and a contact. E-beam evaporation is utilized for Cr, to promote binding between Ag and Al, and for Al, to create the final contact and avoid oxidation of the metal stack. The solar cell area is defined using a mask made up of 30 4x4 mm^2 squares. Because the deposition of the semiconductor layers isn't exactly uniform, solar cell performance varies over the active cell area. By splitting the overall area into 30 smaller cells, it is possible to identify areas with greater or worse performance that would otherwise be averaged out. Absolute current just has to be big enough to be reliably measured.

3.2. Intrinsic layer characterization

3.2.1. Spectroscopic ellipsometry

Spectroscopic ellipsometry (SE) is a measurement technique that involves determining the phase and amplitude of the p- and s- polarizations (parallel and perpendicular) of light reflected by a material. Samples are typically thin films placed on a substrate. It then compares these characteristics with models to determine material attributes such as refractive index (n), film thickness, roughness, and optical bandgap. The SE measuring

equipment utilized in this study was an A M-2000 Ellipsometer made by J.A. Woollam Co.

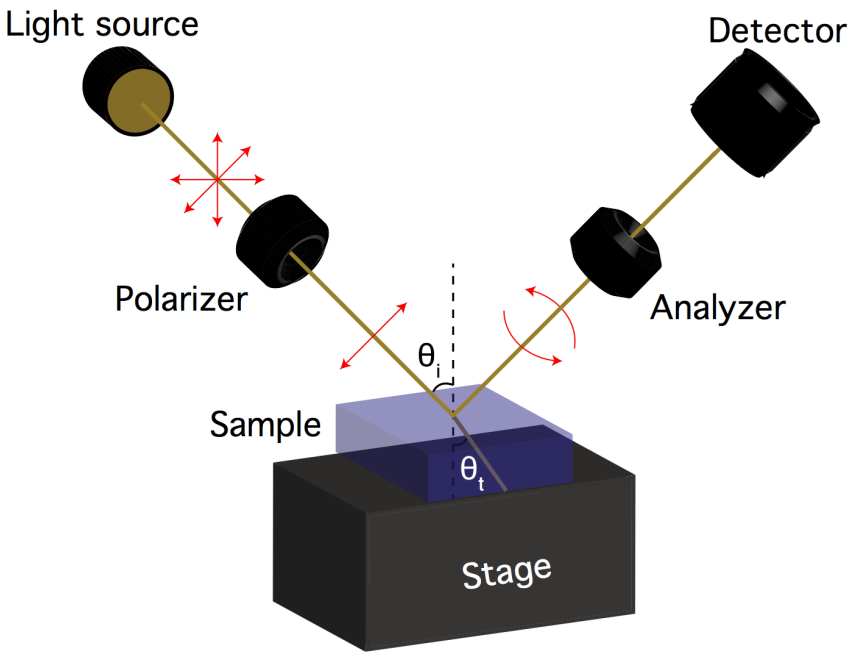


Figure 3.3: Energy band diagram of a p-i-n junction [51]

Refractive Index

The refractive index indicates how much the substance bends light. This can impact the path length of light, therefore a substance with a higher refractive index can slow down light propagation. The real part of the refractive index is often represented by the sign n. This number is critical in determining the optical properties of the film and is sometimes used as an approximate estimate of the film's density [59]. Cody-Lorentz fitting is used to model the data. The refractive index varies according on the wavelength of light. This means that some materials might allow red light to move quicker than blue light. As a result, various materials have varied degrees of reflection across the electromagnetic spectrum. Thus, selecting one wavelength to use for measurements is critical. Previously, in Germanium deposition, $n_{@600nm}$ was utilized as an indicator of material density in thin evaporated films [60] and hydrogenated silicon [61]. For this experiment, $n_{@1400nm}$ was employed since germanium has a low band-gap and it absorbs red and near-infrared light which is closer to 1400 nm than 600 nm.

Absorption coefficient

Spectroscopic ellipsometry quantifies the polarization state of light reflected of a sample surface using the parameters ψ and Δ. These observed characteristics are connected with complex Fresnel reflection coefficients, which are determined by the material's optical properties. Modeling the collected data yields the complex refractive index N = n - ik, wherein n is the refractive index and k is the extinction coefficient. The equation below directly relates the absorption coefficient α to the extinction coefficient k.

$$\alpha = \frac{4\pi k}{\lambda} \tag{3.1}$$

where λ represents the wavelength of light. As a result, after the extinction coefficient k is determined using ellipsometry measurements and modeling, the absorption coefficient may be estimated using the method above [62] .

Bandgap and Thickness

Furthermore, spectroscopic ellipsometry may be utilized to investigate complicated, multi-layered formations. By carefully modeling the interaction of light with each layer, one may determine the thickness and optical bandgap of individual layers inside the structure. The optical bandgap E_{04} represents the amount of energy at which the absorption coefficient hits 10^4 cm^{-1}.

3.2.2. Activation Energy and Dark conductivity

The activation energy (E_{act}) is the minimal energy needed to release an electron out of its bound state and enable it to flow freely inside the material [63]. To be an efficient absorber material, the energy required for activation must be within a certain range. If the activation energy is too great, only high-energy photons can form electron-hole pairs, leading to low efficiency and underutilization of lower-energy photons. However, if the activation energy remains too low, thermal energy alone might be sufficient to free electrons, resulting in high leakage currents and lower efficiency. For intrinsic materials, the value should be close to half of the material's bandgap (E_g) [64].

The activation energy can be influenced by various factors, such as the material's band

structure, impurities, and defects. It is typically determined experimentally by analyzing the temperature dependence of the material's electrical conductivity. To measure the dark conductivity, 300nm-thick parallel electrodes made of aluminium were evaporated onto the germanium thin films. Samples were annealed at 130°C for 45 mins to fix the contacts. Dark conductivity (σ_d) was then obtained by current measured at different temperatures descending from 130°C to 60°C in intervals of 5°C. A voltage of 10 V was only applied when the temperature was stabilised, after which the current is measured, and then calculate the resistance, and then the conductivity. The samples were placed in a dark environment. Activation energy and pre-exponential factor σ_0 can then be calculated by the Arrhenius equation:

$$\sigma_d = \sigma_0 exp(\frac{-E_{act}}{k_b T}) \tag{3.2}$$

In order to obtain E_{act} , a curve of ln $(1/\sigma_d(T))$ over $1/k_B T$ is drawn, then the slope of the fitted straight line indicates the E_{act} for which an example is shown in Figure 3.4.

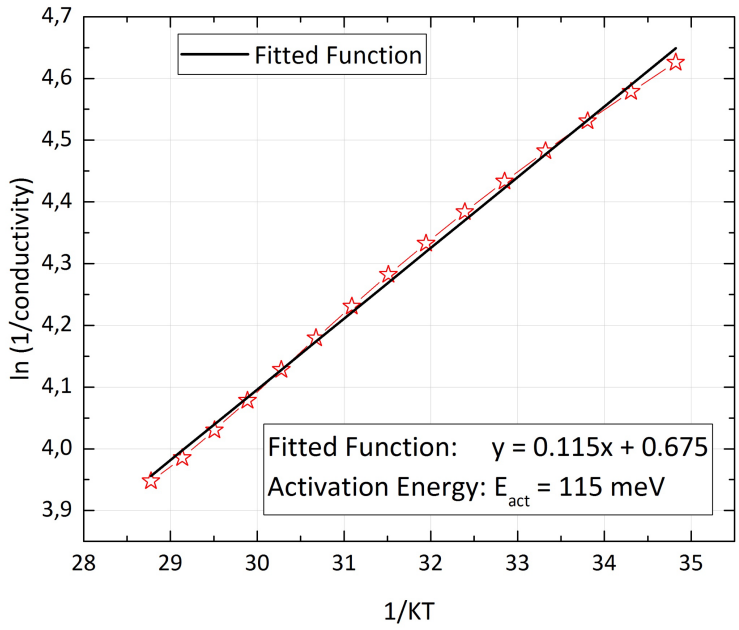


Figure 3.4: An example of activation energy calculation [65]

3.2.3. Raman Spectroscopy

Raman Spectroscopy is a technique for determining the structure of a material by examining inelastic scattering of photons. It entails lighting a sample with a laser before detecting and analyzing the dispersed light. The dispersed light contains data pertaining to the vibrational modes of the molecules that are in the sample, revealing their chemical makeup and molecular bonding. In this study, measurements were taken using an InVia confocal Raman Renishaw microscope and an Argon red laser at a wavelength of 638 nm. The spectra are fitted using Gaussian distributions at Raman shifts of 177 cm^{-1}, 230 cm^{-1}, and 278 cm^{-1} that correspond to amorphous germanium stretching modes [66], and another Gaussian at 300 cm^{-1} for the crystalline germanium peak at 300 cm^{-1} [67]. The Gaussians are fitted using the freeware Fityk [68].

3.2.4. Fourier Transform Infrared Spectroscopy (FTIR)

Fourier Transform Infrared Spectroscopy (FTIR) is an effective method for material characterisation. It entails studying the material's reaction with infrared light to determine its chemical composition and structural qualities. FTIR may offer extensive information on chemical bonds and functional groups by exposing the material to a wide range of infrared wavelengths and using a mathematical approach known as the Fourier transform. This data is critical for assessing the efficiency and performance of solar cells since it identifies impurities, flaws, and degradation mechanisms that may impair their overall functioning.

To produce the samples for this test, germanium is deposited onto (100) oriented crystalline silicon wafers. These wafers are then compared to a sample crystalline silicon wafer from the exact same batch to eliminate the background spectrum. This test identifies the existence of oxygen induced by germanium oxidation, demonstrating the material's chemical stability. Ge:H wagging mode occurs at 560-580 cm^{-1}, Ge:H Low stretching mode (LSM) at 1875 cm^{-1}, and High stretching mode (HSM) at around 1980 cm^{-1} [69] [13] [70]. Figure 3.5 depicts a typical FTIR spectrum of an oxidized germanium film.

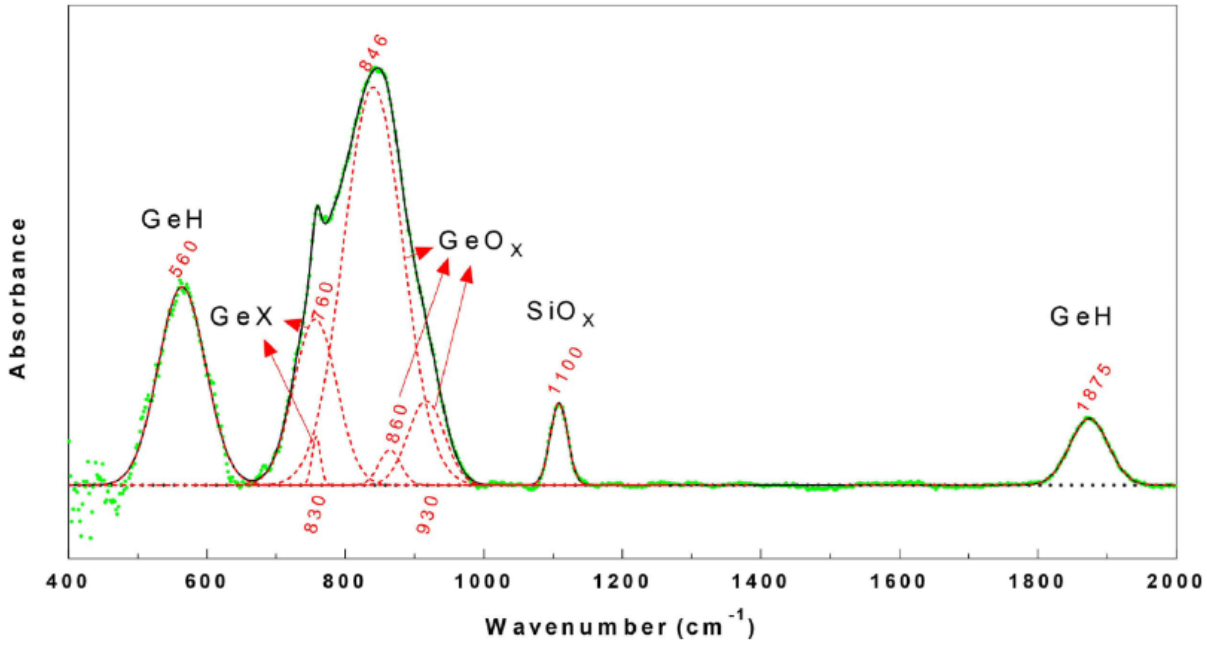


Figure 3.5: Fitted FTIR spectrum of a Ge:H film after oxidation [13]

3.3. Characterization of solar cell performance

3.3.1. J-V curve measurement

The solar cell's electrical performance is assessed by measuring its lighted J-V characteristics utilizing a Wacom WXS-90S-L2, class AAA, dual-lamp solar simulator. To ensure accurate measurements under Standard Test Conditions, the measuring stage is temperature regulated and the filtered spectral output is calibrated to 1000 W/m^2 using two mono-crystalline silicon reference cells calibrated by the Fraunhofer Institute for Solar Energy Systems. The setup beams light perpendicularly on a sample while automatically adjusting a resistive load to follow the J-V curve of the solar cell. This curve provides direct measurements of J_{SC} and V_{OC} at close to zero and infinite load, respectively. The FF and conversion efficiency are computed using J_{SC}, V_{OC}, and P_{max}. R_S and R_{SH} are computed by extrapolating the trend of the J-V curve towards open-circuit and short-circuit, respectively.

4

Results

4.1. Suitable conditions for intrinsic Germanium films

To find out the ideal conditions for obtaining intrinsic germanium layers, various deposition parameters have been varied. Several deposition parameters were tweaked to obtain a stable regime and achieve high quality germanium absorber layer. The parameters that were explored were pressure, RF power, temperature and germane flow ratio. The parameters that are used to characterize ideal deposition conditions are the bandgap, refractive index, activation energy, and absorption coefficient.

4.1.1. Effect of Temperature

In this experiment the substrate temperature was varied to find out its effect on the opto-electrical properties. It is essential to explore the lower temperature regions as even though literature supports that higher temperatures yield better germanium films, these high temperatures can lead to complexities while producing a solar cell. There is a possibility that the doped layers of the cell would be destroyed upon exposure to high temperature. The pressure, power, germane and hydrogen flows and electrode distance were kept fixed at 4 mbar, 12 W, 3 sccm, 200 sccm, and 13 mm.

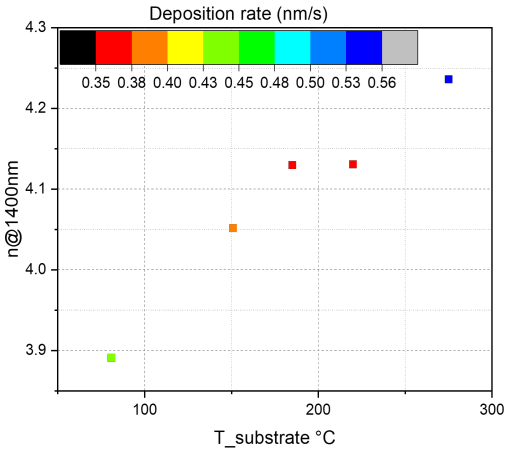


Figure 4.1: Change in refractive index and deposition rate with substrate temperature

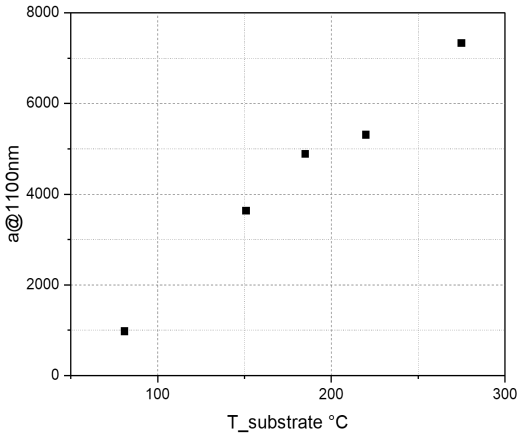


Figure 4.2: Change in absorption coefficient with substrate temperature

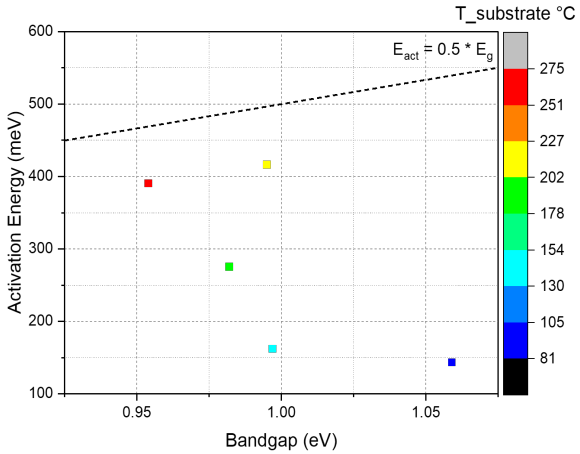


Figure 4.3: Intrinsicity of amorphous germanium with change in substrate temperature

From Figure 4.1 it can be seen that the refractive index increases with an increase in temperature which goes to show that with a higher substrate temperature the germanium layer possesses denser material properties. This finding is in line with that of de Vrijer et al [13]. The samples were not deposited at temperatures higher than 275 °C as the germanium films are to be utilised in a single junction solar cell with p and n layers which can not withstand very high temperatures, so going beyond these temperatures to develop an intrinsic germanium layer would guarantee the damage of the p and n layers when this recipe would be coupled with that of the solar cell. It was also seen that with an increase in substrate

temperature the deposition rate of the sample increased. Even the absorption coefficient increased linearly with the substrate temperature which signifies that the Germanium layer will absorb a higher portion of the incident sunlight compared to the samples produced at lower substrate temperatures. Figure 4.3 also shows that the bandgap decreases with an increase in temperature. Higher deposition temperatures allow for more structural relaxation during growth. This relaxation can lead to a reduction in internal stress and a corresponding decrease in the bandgap [71]. From Figure 4.4 it is observed that there is a higher concentration of defects and contamination being oxygen. The FTIR characterization is carried out as it provides an understanding regarding the presence of contaminants and the kind of bonds that are present between the atoms. FTIR spectra of 5 samples pertaining to different temperatures varying from 81 °C - 275 °C is shown in Figure 4.4. It also shows that the concentration of oxygen reduces with an increase in deposition temperature. Higher deposition temperatures can reduce the density of defects in the amorphous structure. Fewer defects lead to a narrower distribution of localized states in the bandgap, effectively reducing the optical bandgap [72]. The densification of the films results in more stable films with a higher activation energy [70]. It can be seen that the material is most intrinsic meaning that the activation energy is around half of the bandgap; is for samples produced at 225 and 275°C. It was found that the samples with a higher substrate temperature were intrinsic.

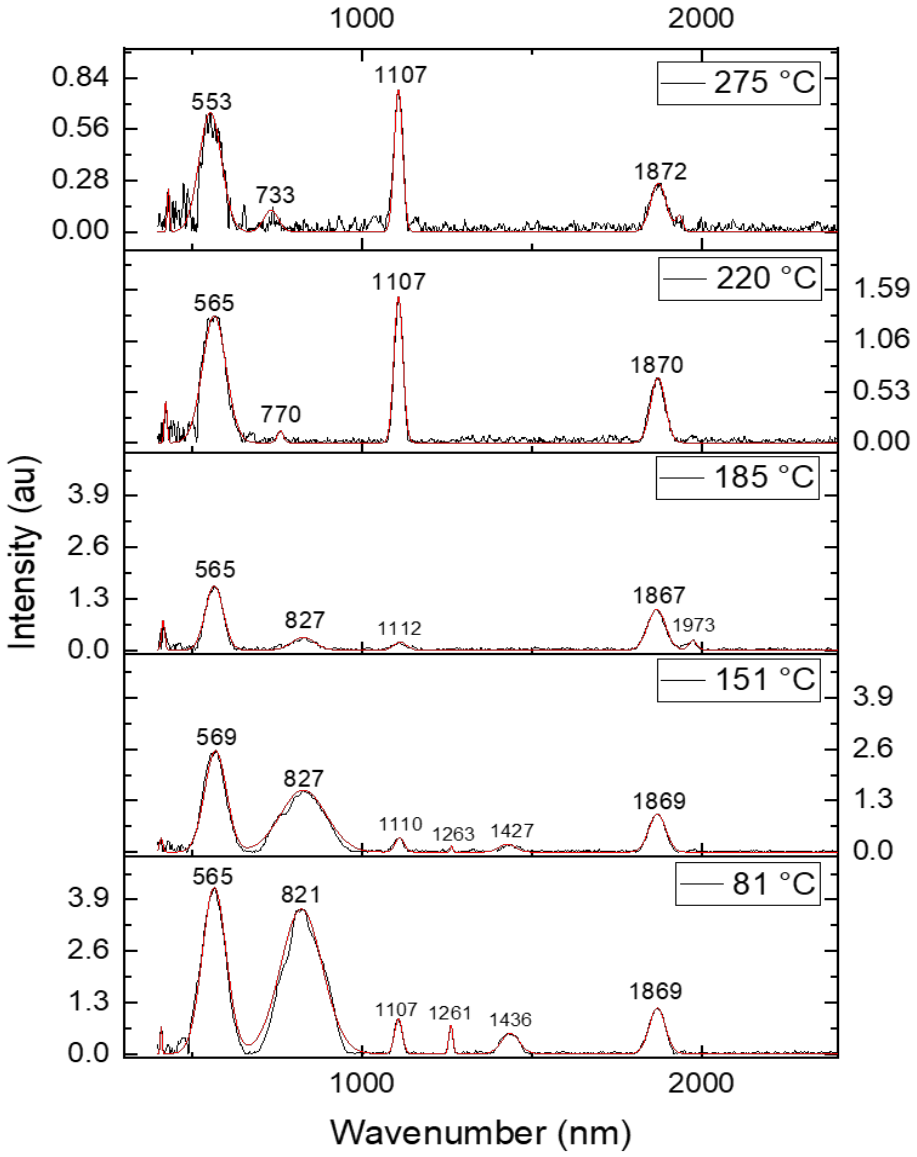


Figure 4.4: Material characteristics of the amorphous germanium samples with change in temperature

4.1.2. Effect of GeH_4 flow on optoelectrical properties

In this case only the germane flow is varied and the hydrogen flow is kept constant at 200 sccm, since this is the maximum the mass flow controller would allow. A series of 5 samples were used for this experiment varying the germane flow from 1 to 5 sccm. A germane flow of 1 sccm was kept at minimum as a crystalline phase had been observed for at an

$F(H_2)/F(GeH_4)$ of 400 (the hydrogen flow at 200 sccm and germane flow at 0.5 sccm) as given in [13]. The experiment was carried out while keeping the parameters pressure, power, substrate temperature and electrode distance constant at 4.5 mbar, 12 W, 275 °C and 13 mm, respectively.

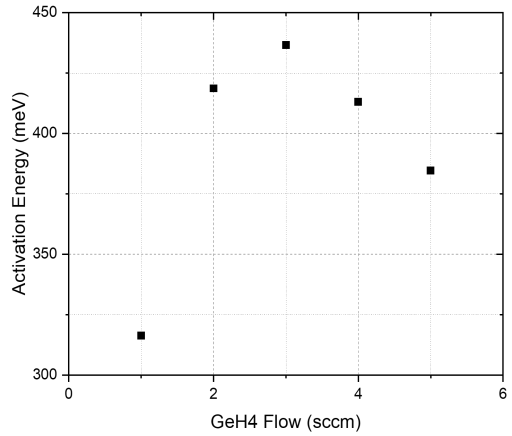


Figure 4.5: Change in activation energy with variation in germane flow

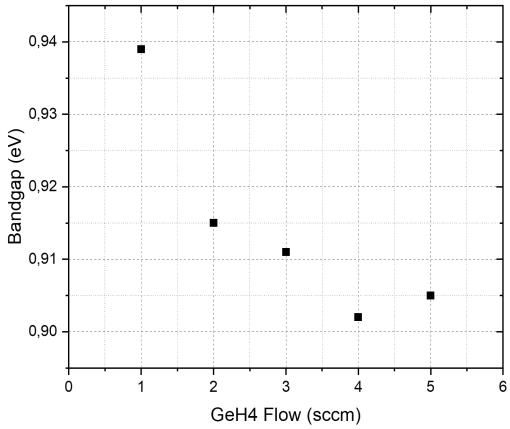


Figure 4.6: Change in band-gap with variation in germane flow

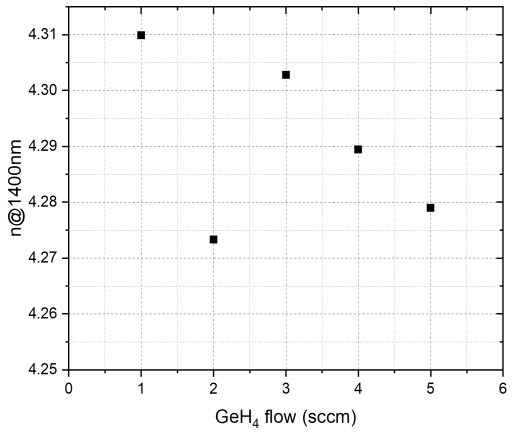


Figure 4.7: Change in refractive index with variation in germane flow

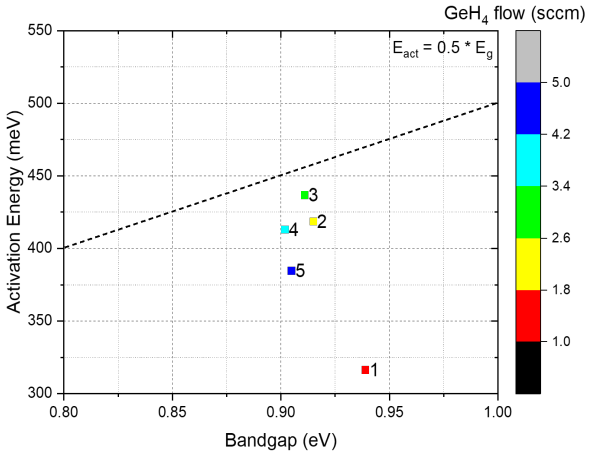


Figure 4.8: Intrinsicity of amorphous germanium with variation in germane flow

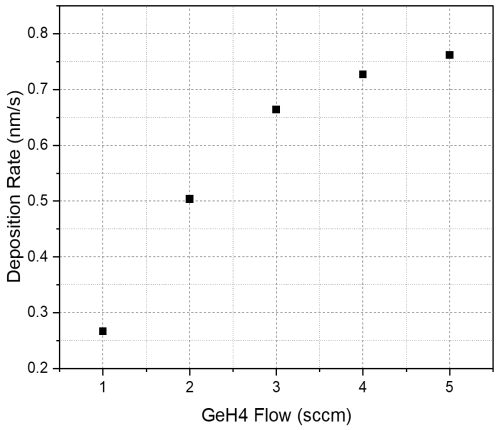


Figure 4.9: Changes in the deposition rate of the amorphous germanium with variation in germane flow

From Figure 4.5 it is seen that by varying the Germane flow the activation energy was the highest at 3 sccm while the band-gap dropped till 2 sccm and then there was hardly any change in the band-gap till 5 sccm which is seen in Figure 4.6. Increasing the flow of Germane during deposition causes a larger concentration of germanium in the resultant amorphous layer and a higher deposition rate is observed. When the germane content increases, resulting in a decreased fraction of passivated Ge dangling bonds, the defect density is increased. As the germanium defect states have energy levels that have energy levels closer to the conduction band, the material becomes a bit more n-type resulting in decreased activation energy [73]. When the germane content increases the refractive index of the material decreases and is in line with previous findings [13]. The decrease in refractive index indicates an increase in porosity. The refractive index depends on the hydrogen content and with a decrease in the hydrogen/germane flow ratio the material becomes less dense [74]. It can be seen from Figure 4.8 that the germanium layer deposited at 3 sccm is the most intrinsic. The layers deposited at higher and lower flow rates leaned more towards the n side making them unsuitable to be used in the intrinsic absorber layer. Furthermore, FTIR characterization was done on the samples to understand the presence of voids and the germane and hydrogen content. From the FTIR spectra shown in Figure 4.10 it is observed that the germane flow at 1 sccm displays a HSM at 1922 cm^{-1} indicating the presence of

voids in the sample. The hydrogen associated with HSM vibrations is located at the surface of bigger nano-sized voids in the amorphous germanium lattice [70]. With increasing the germane flow as the deposition rate increased which indicates that the amorphous layer's thickness increases too. The increase in thickness is one of the reasons that the Ge:H peaks at 560-570 cm^{-1} increase with increasing germane content. The LSM of the samples deposited at varying germane flow have around the same intensity and as the LSM is also indicative of voids which are a type of structural defect; it could potentially influence the band-gap by affecting the density of states, which is in line with why the band-gap of the samples does not vary by much.

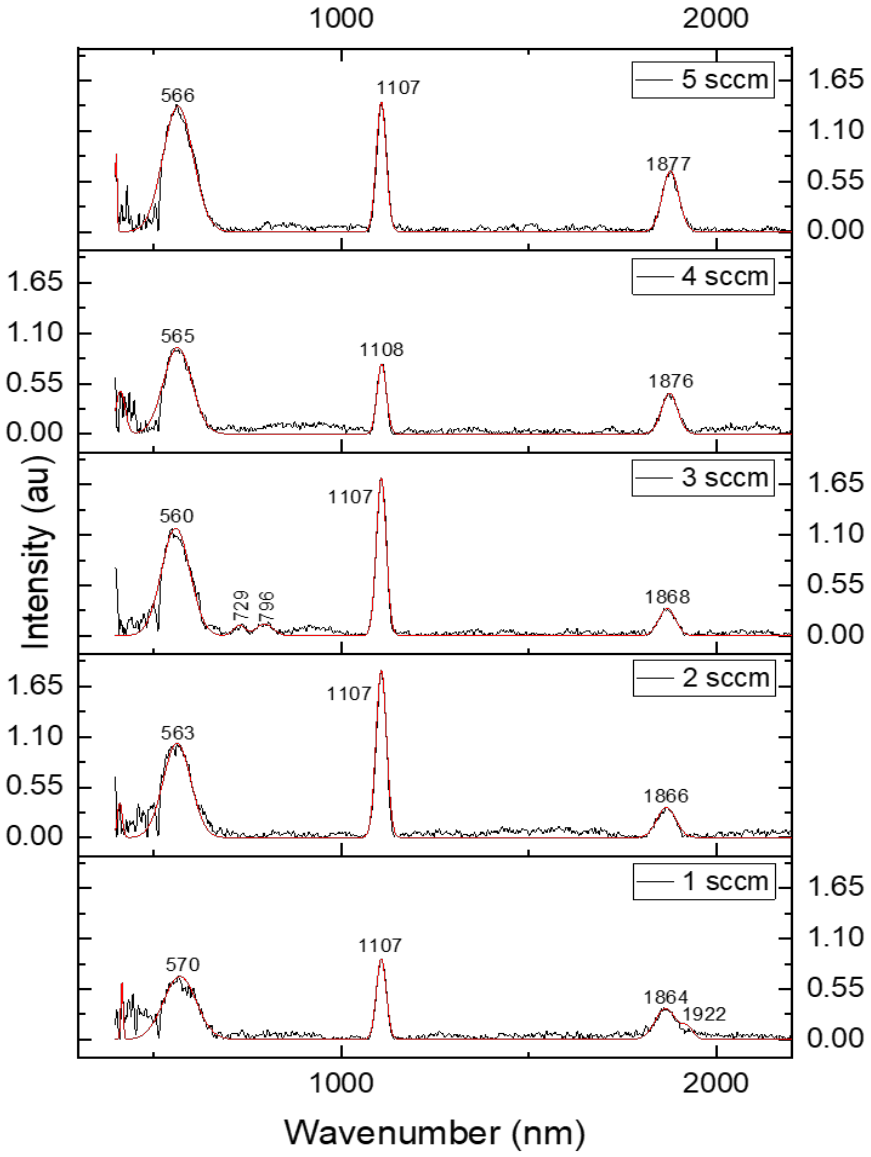


Figure 4.10: Material characteristics of the amorphous germanium samples with change in germane flow

4.1.3. Effect of Power and Pressure

The effect of power and pressure variations were now studied across 25 samples. The interplay between power and pressure during deposition can influence the characteristics of the resultant amorphous germanium films. Finding the optimum power-to-pressure ratio is critical for obtaining desirable film characteristics and deposition rates while avoiding

difficulties like target damage or excessive gas phase reactions [75]. Other important parameters such as hydrogen flows, electrode distance and deposition time were kept constant.

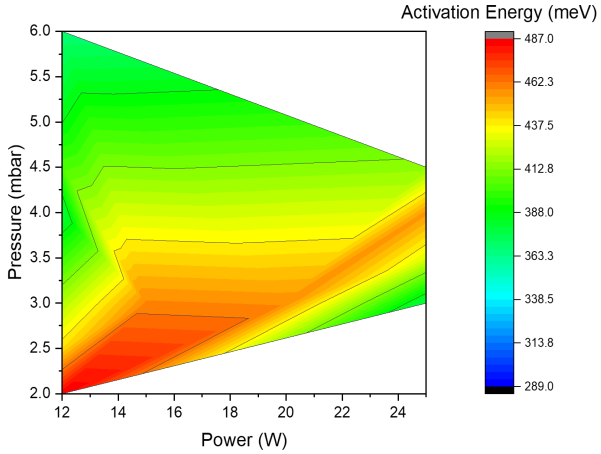


Figure 4.11: Impact of the pressure and power on activation energy

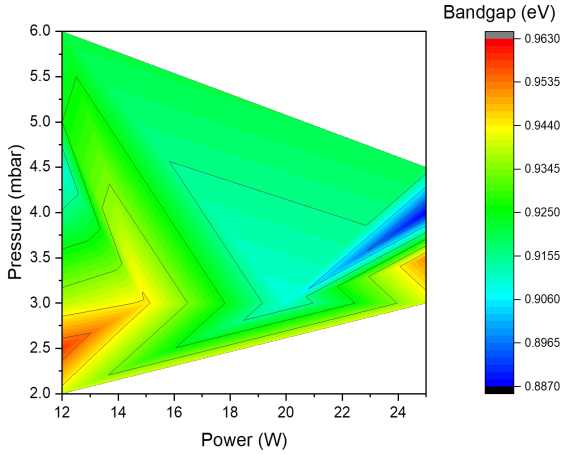


Figure 4.12: Impact of the pressure and power on the bandgap

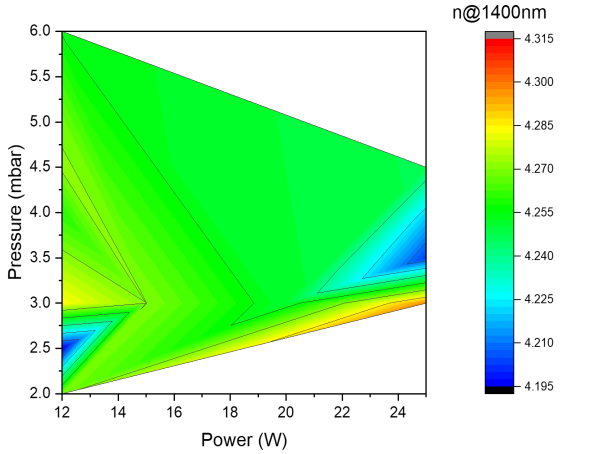


Figure 4.13: Impact of the pressure and power on the refractive index

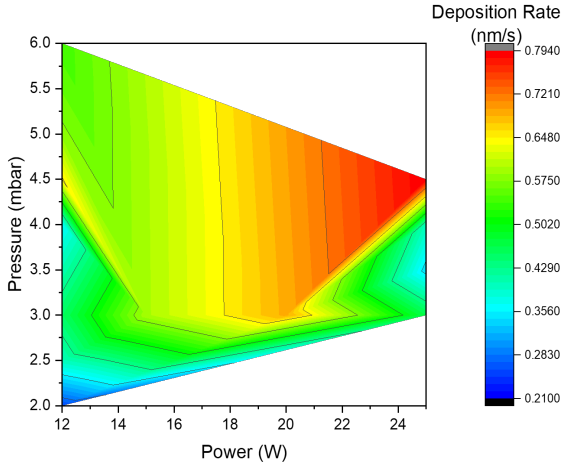


Figure 4.14: Impact of the pressure and power on the deposition rate

From these measurements it is observed that the activation energy is higher for lower pressures and at a low RF power which is shown in Figure 4.11. Whereas, Figure 4.12 shows that the bandgap is low at higher powers. So to develop an intrinsic layer, the pressure and powers have to be optimized. The pressure and power have to be varied such that the germanium layer has a low band-gap, while having a high activation energy that accounts to

almost half of the band-gap. From Figure 4.11 it can be inferred that a low pressure till about 2-4 mbar and a power of 12-20 W would provide a layer with a high activation energy. For obtaining a sample with a low bandgap, pressures of 2-4.5 mbar and power range of 18-25 W have to be explored. The deposition rate increases with increasing power while pressure also affects the deposition rate depending on the power level [76]. From Figure 4.13 it can be seen that the refractive index does not vary with power and pressure as the refractive index of amorphous germanium is primarily determined by the order of its structure which is influenced by the deposition temperature.

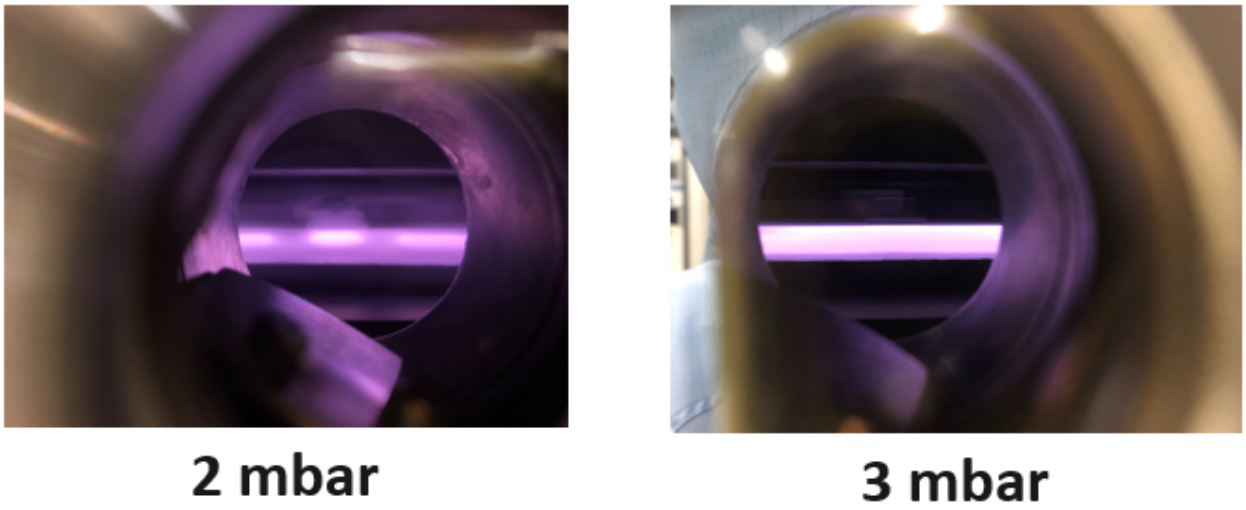


Figure 4.15: Plasma at different pressures

The region of low pressures is not considered suitable for germanium deposition as the plasma looks unstable which can be seen in Figure 4.15. In the plasma at 2 mbar small gaps can be seen but at 3 mbar a stable plasma is observed which is suitable for deposition.

4.1.4. Effect of Pressure

In this case, solely pressure was varied across 11 samples, all other deposition parameters were kept constant. The substrate temperature was kept at 275 °C and the power was kept constant at 12 W as the samples were homogeneous at this power as stated in previous sections and also seen in previous research.

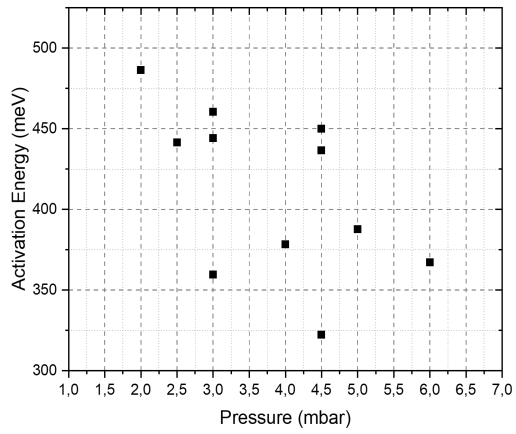


Figure 4.16: Change in activation energy with variation in pressure

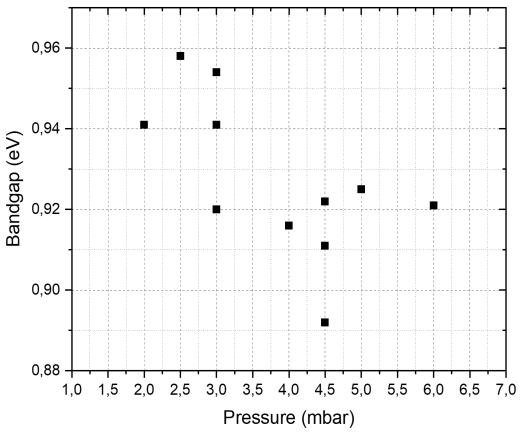


Figure 4.17: Change in band-gap with variation in pressure

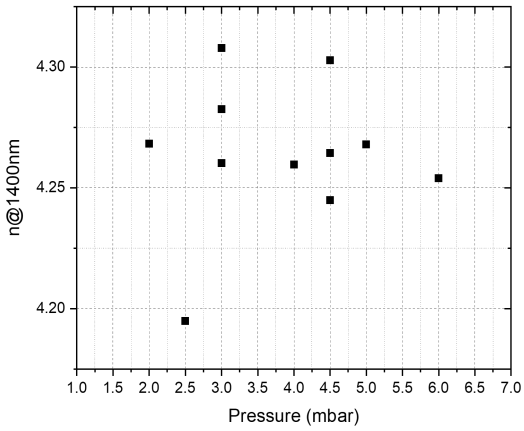


Figure 4.18: Change in the refractive index with variation in pressure

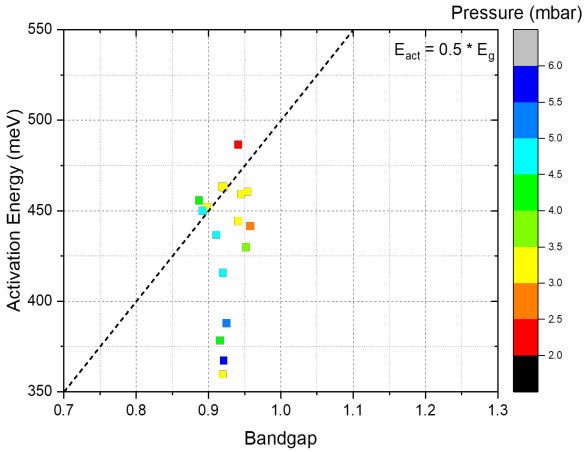


Figure 4.19: Intrinsicity with variation in pressure

These measurements showed the the activation energy was highest at lower pressures and bandgaps were low at higher pressures. The refractive index has hardly any change with pressure but it is observed that the refractive index is highest at 3 mbar and 4.5 mbar. The pressures lower than 4-4.5 mbar give intrinsic materials, and lower pressures have not been opted because then the bandgap increases, so it is beneficial to stay within the 4.5-3 mbar range to achieve a good layer.

4.1.5. Effect of Power

From the previous experiment it was found that pressures of around 3-4.5 mbar. To further back this finding the samples deposited at 3 mbar were studied. These samples were deposited at a constant substrate temperature, electrode distance and germane and hydrogen flows of 275 °C, 13 mm, 3 and 200 sccm.

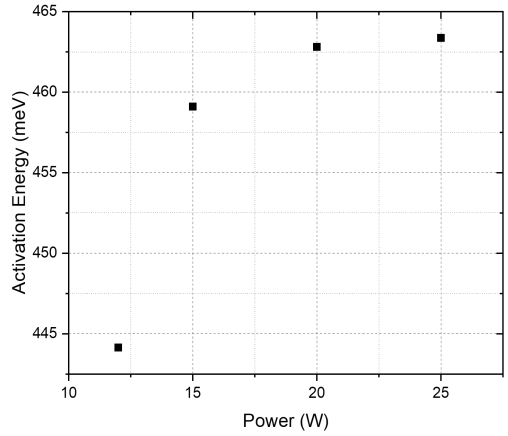


Figure 4.20: Change in activation energy with variation in power

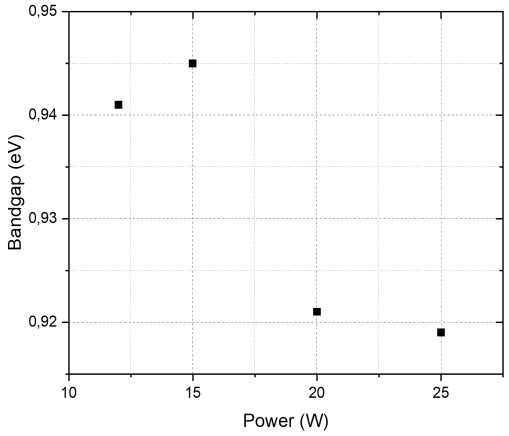


Figure 4.21: Change in the bandgap with variation in power

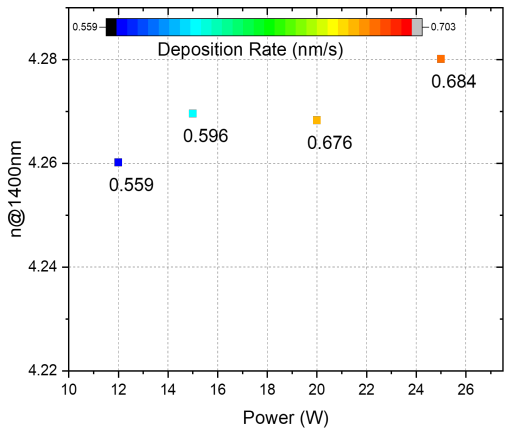


Figure 4.22: Change in the refractive index with variation in power

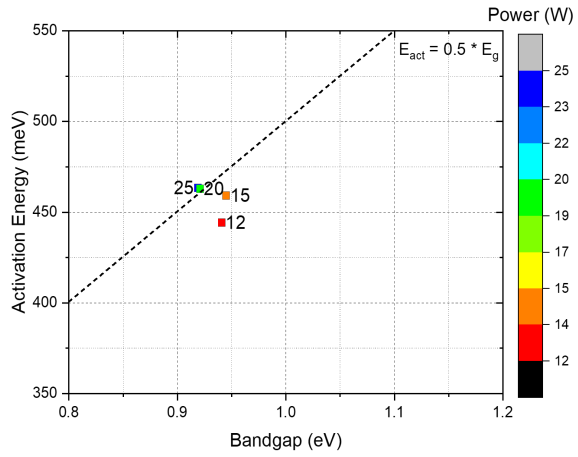


Figure 4.23: Intrinsicity of the amorphous germanium with variation in power

From Figure 4.20 it can be seen that the activation energy of the germanium increases with an increase in power and bandgap decreases with an increase in power as seen in Figure 4.21.

As the deposition rate increases with power, the germanium content increases the absorption increases, thereby decreasing the bandgap [18]. From the characterization of the material done through FTIR shown in Figure 4.24 it can be seen that there is an increase in impurities in the sample with an increase in power, with the impurities being GeO_x spanning from around 650-950 cm^{-1} which is also seen in literature. Deposition power could potentially influence the incorporation of impurities or the formation of defects, which in turn could affect the activation energy and bandgap [77]. With an increase in the deposition power there is an increase in the deposition rate which does not have an impact on the refractive index of the material as seen in Figure 4.22. As even though it might appear that there is an increase in the refractive index with an increase in deposition rate, the change is very minimal which can be the result of measurement errors. From Figure 4.23 it can be seen that the material is the most intrinsic at high powers.

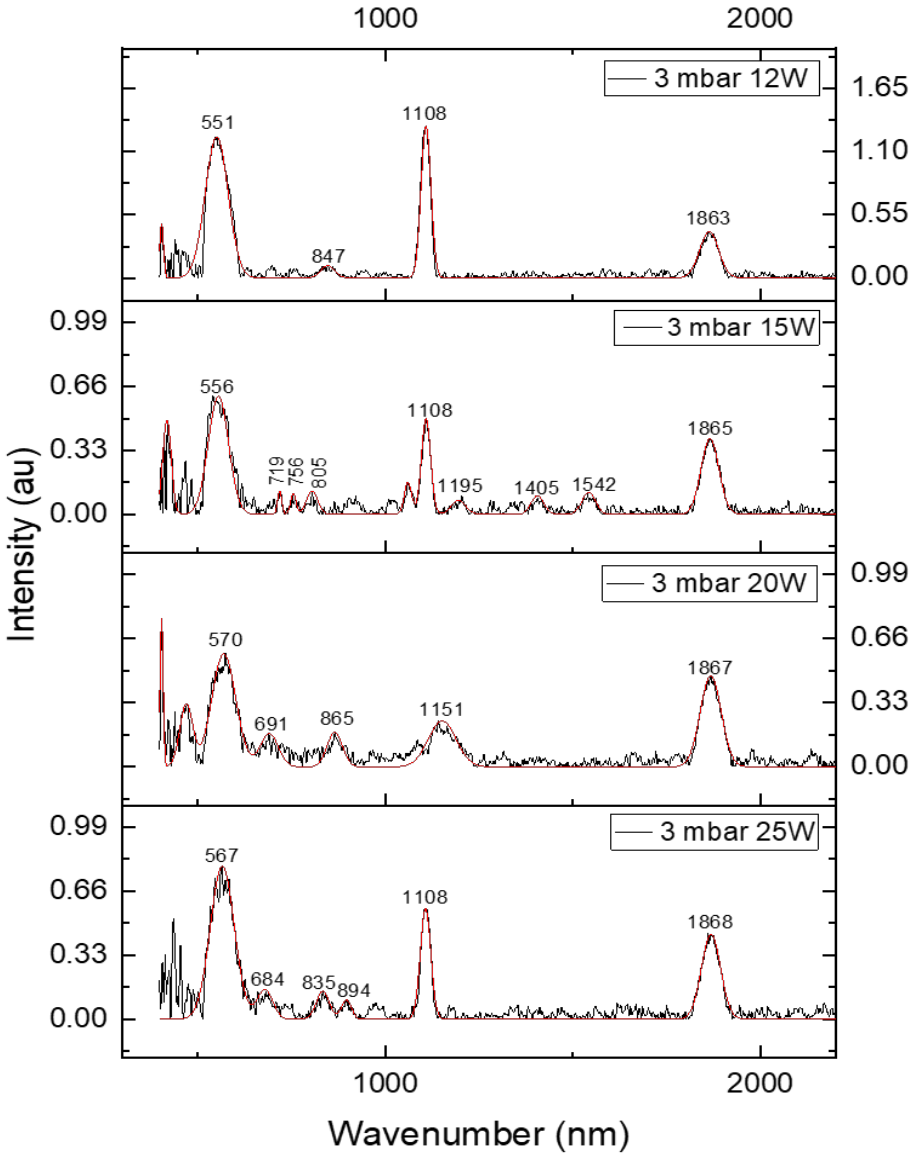


Figure 4.24: FTIR characterization of the samples deposited at 3 mbar at varying powers

4.2. a-Ge:H single junction device

Proper bandgap engineering makes sure that the energy bands line well across layers. This promotes effective charge separation and lowers recombination loss at interfaces. The bandgaps for various layers in a p-i-n solar cell with buffer layers and a TCO may be carefully engineered to maximize charge separation, light absorption, and carrier collection.

This results in higher overall cell performance and efficiency across a broader range of operating circumstances.

4.2.1. Device architecture

Upon exploring the optimum deposition conditions of the Germanium layer, these conditions were transferred to the germanium deposition in a single junction configuration. The first cell was deposited in a p-i-n configuration with buffer layers at the interfaces between p and i layer and i and n layer. The solar cell uses a p-i-n superstrate configuration deposited on the Asahi VU with FTO as TCO. To prevent reduction of the FTO TCO by the hydrogen rich plasma that is present during p-layer deposition, a thin i-ZnO layer is deposited on the TCO [78]. Figure 4.25 depicts the configuration of the solar cell along with its J-V characteristics.

A p layer of nc-SiO_x:H is employed in this cell as the high optical bandgap minimises the parasitic absorption. Hydrogenated nanocrystalline silicon oxide (nc-SiOx:H) with lower absorption coefficient than the a-Si:H counterpart is promising to improve J_{SC} when utilised as the window layer of solar cells [48].

The buffer layer is introduced to avoid diffusion of hydrogen and boron out of the p layer and passivate the surface from dangling bonds that arise due to differences in the lattices. Intrinsic i-a-Si:H buffer barriers are embedded on both sides of the a-Ge:H nanoabsorber to reduce strains and defects occurring at the interfaces of doped layers. The buffer layer is chosen as the thinnest possible that will still give full coverage (i.e. be pinhole free), since the thinner it is the lesser the parasitic absorption, and the charges can tunnel through it so it does not add barriers to the structure. The buffer layer thicknesses also aid in avoiding a band gap change due to quantum size effects in the barriers [79]. Both a-Ge:H and a-Si:H matrix consist of tetrahedral covalent random network and lattice-matched bonds length [80], [81]. This leads to atomically abrupt a-Si:H/a-Ge:H interface consisting of a monolayer of randomly mixed Si and Ge linked to homopolar thin film with low density of defects, ensuring the preservation of layer bulk properties [80], [81],[82]. This redistributes the space charges near the p/i and i/n interfaces which smooths the electric field and enhances the charge collection. Adding 5 nm to the p/i buffer would improve the performance the most

in terms of V_{OC} , but suffers a loss in J_{SC} that results in a slight increase of conversion efficiency [48].

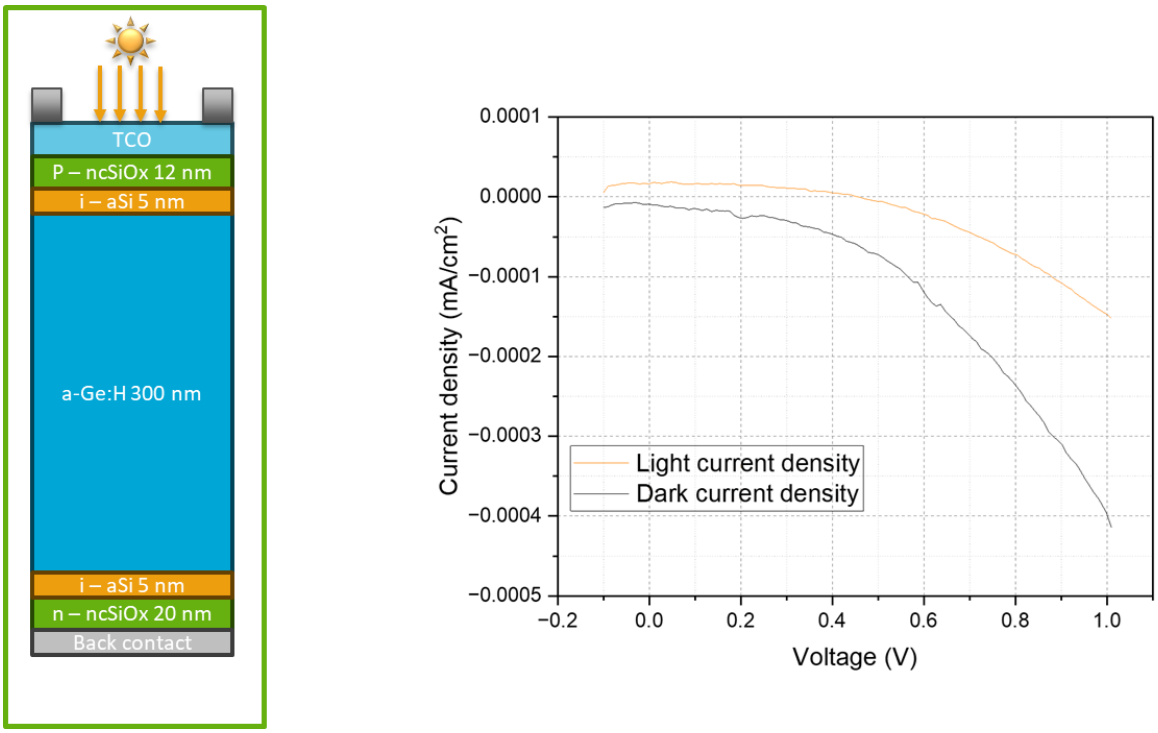


Figure 4.25: J-V characteristics of the cell deposited in the p-i-n configuration

Upon measuring the J-V characteristics of the solar cell shown in Figure 4.25 it was found that the cell displayed diode characteristics but the current density was very low. There was very little difference in the light and dark current density. This configuration was repeated again with varying absorber thicknesses varying from 300 nm to 20 nm. The absorber thickness is reduced as the shorter the distance that the photogenerated carriers need to travel in an absorber, lesser is the likelihood of recombination, permitting more minority carriers to be collected efficiently and a higher carrier density is observed too [83]. The J-V characteristics of the cells with the same device architecture as Figure 4.25 and varying thickness is shown in Figure 4.26.

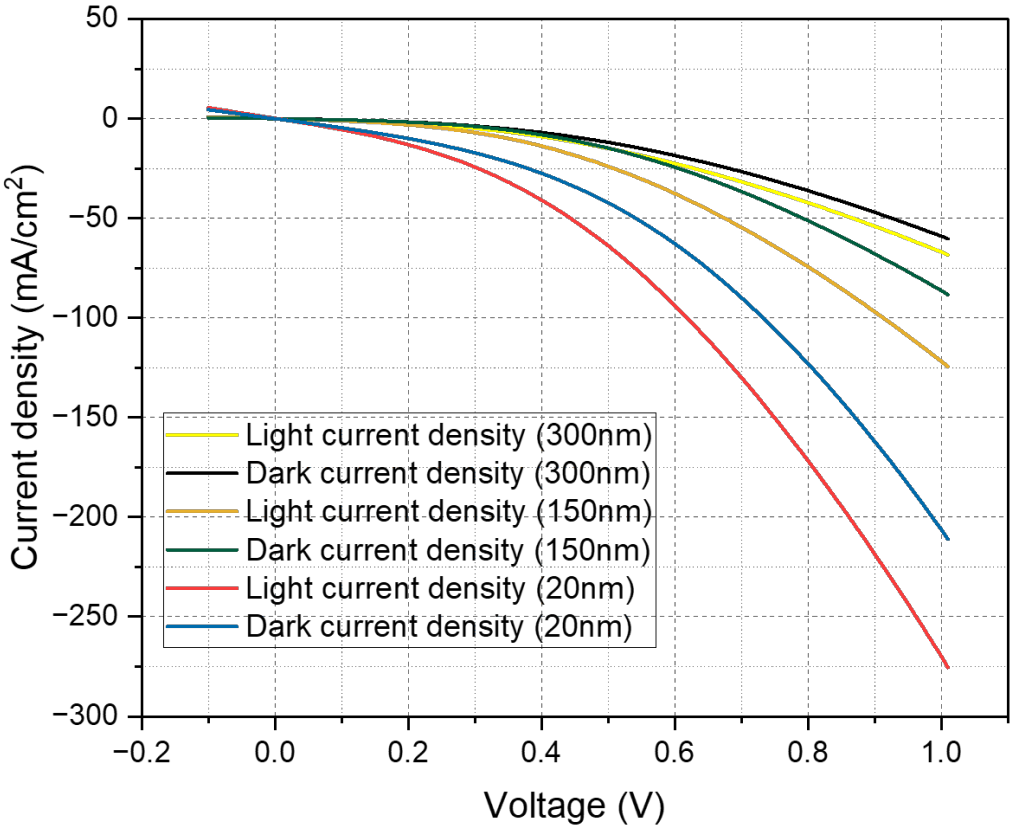


Figure 4.26: J-V characteristics of p-i-n configuration cells with varying thicknesses

From Figure 4.26 it can be seen that the current density has increased with a decrease in thickness of the absorber which is in line with [83]. Due to reduced thickness of the absorber thermal emission over the potential barrier is the dominant hole conduction mechanism at the a-Si:H/a-Ge:H hetero-interface [84][85]. However, like the Figure 4.25 the difference in the light and dark current density is low. It was speculated that there was less charge carrier collection due to the presence of a barrier at the window layer which is the p layer and high recombination rates of the electron hole pairs before contributing to current.

To validate this finding, a model was made of the used device architecture which is shown in Figure 4.27. From the model it can be inferred that a barrier for hole collection can be seen at the p/i layer of the device which arised due to a large difference in bandgaps and it was

proposed to reduce the bandgap at the p-side of the solar cell.

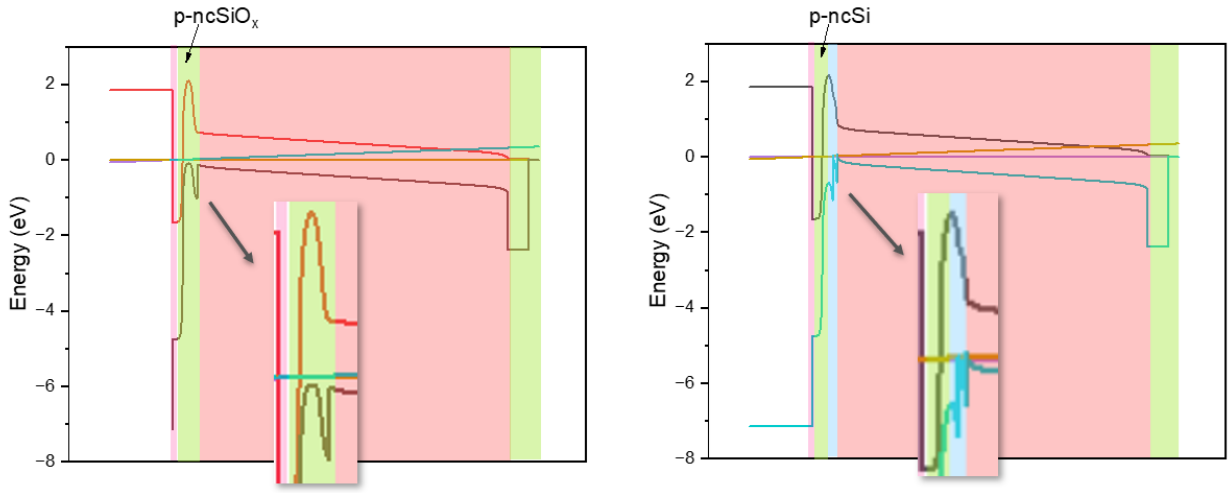


Figure 4.27: Models of the first cell and the prospective cell configuration

Based on these results, the p-layer and i layer were composed of p-type ncSi:H and intrinsic ncSi:H respectively. The p-type nc-Si:H layer has low activation energy similarly to the p-type nc-SiO$_x$:H and produces a good ohmic contact with the front TCO [48]. p-type ncSi:H layer has been chosen as it has a higher conductivity compared to p-ncSiO$_x$:H. The incorporation of oxygen in nc-SiO$_x$:H can reduce the conductivity of the material [86]. The p-type nc-Si:H layer forms a better interface with other silicon based layers in the solar cell [83]. A thinner absorber layer was used due to higher current density observed in cells with thinner layers as shown in Figure 4.26.

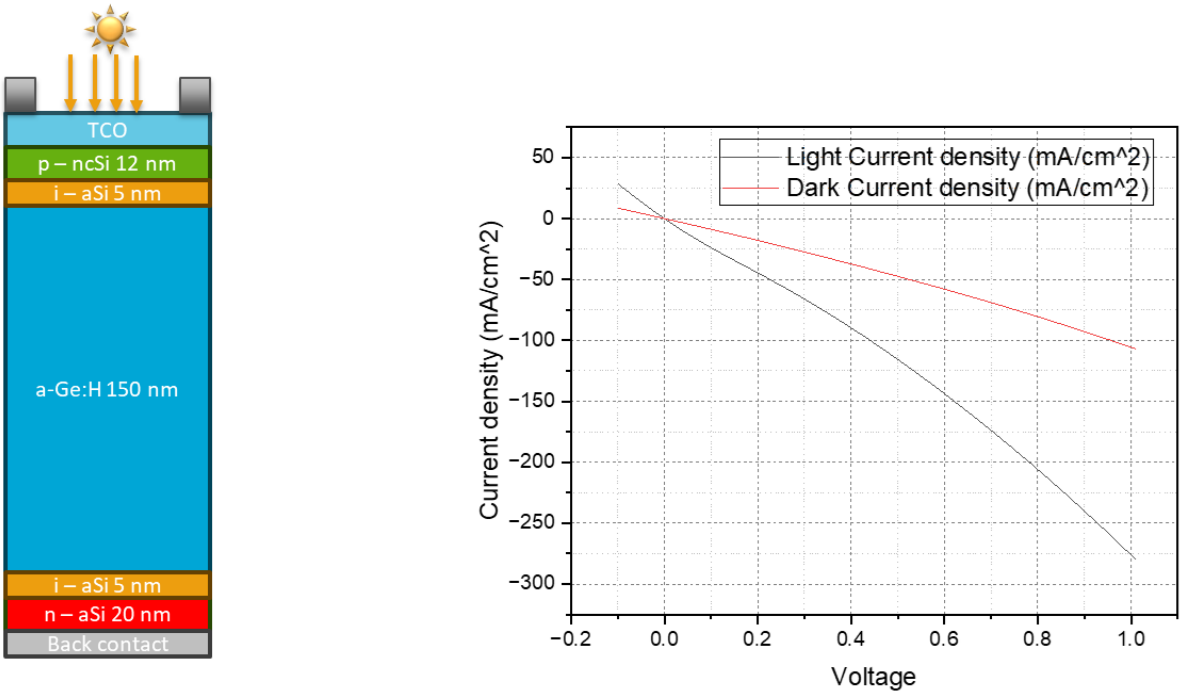


Figure 4.28: J-V characteristics of the cell deposited in the p-i-n configuration with a ncSi p-layer

The Figure 4.28 employs an absorber layer of the same thickness as the Figure 4.29 but the buffer layers are similar to that of the Figure 4.25. Upon changing the intrinsic layer to that of ncSi:H the device still did not show any improvement compared to the previous device but infact this device depicted the signs of a resistor [87].

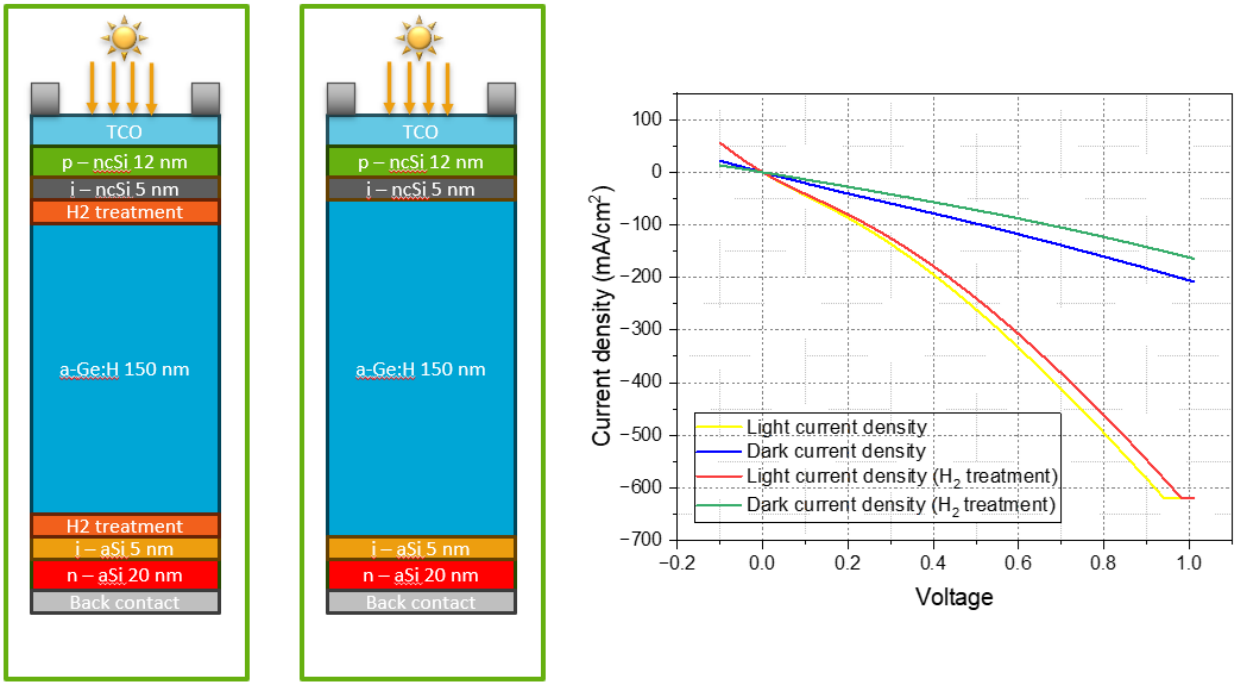


Figure 4.29: J-V characteristics of the cell deposited in the p-i-n configuration with a ncSi p-layer and buffer layer and hydrogen treatment

The cells illustrated in Figure 4.29 utilise the same configuration with the only difference in the cell on the right being in the interface between the buffer layers being passivated using hydrogen. The passivation reduces the dangling bonds present on the surface of the germanium absorber hereby reducing surface recombination [88] and enhacing the carrier collection [89]. If the cell's p-i-n junctions are not well-formed or have a high defect density, they may be unable to efficiently separate and collect charge carriers. This might lead the cell to act more like a resistor than a diode, especially during illumination [28].

As the p-i-n configuration displayed some solar cell characteristics, it was speculated that the n-i-p configuration would show better results as the n-i- configuration potentially provides better thermal and electrical properties which are important for long term stability and efficiency. For the next three cells shown in Figure 4.31 the n-i-p configuration has been utilised with a ncSiO$_x$ n layer, a-Si buffer layer at the n/i interface and a ncSi buffer layer at the p/i interface along with a nc-Si p layer. The absorber layer thickness is kept constant at 50 nm. The only parameter that was varied in these samples was the doping concentration of the p-layer. According to literature higher doping of the p-layer leads to increased

conductivity which positions the Fermi level closer to the valence band resulting in a higher built in voltage and open circuit voltage [90], [91]. Doping the p-layer can enhance the hole collection at the back of the cell, which is important for efficient charge extraction in n-i-p cells [90]. Doping the p-layer instead of the n-layer allows higher conductivity without compromising the optical properties of the window layer [92]. The doping concentration was varied by increasing the B_2H_6 gas flow at 20, 40 and 60 sccm.

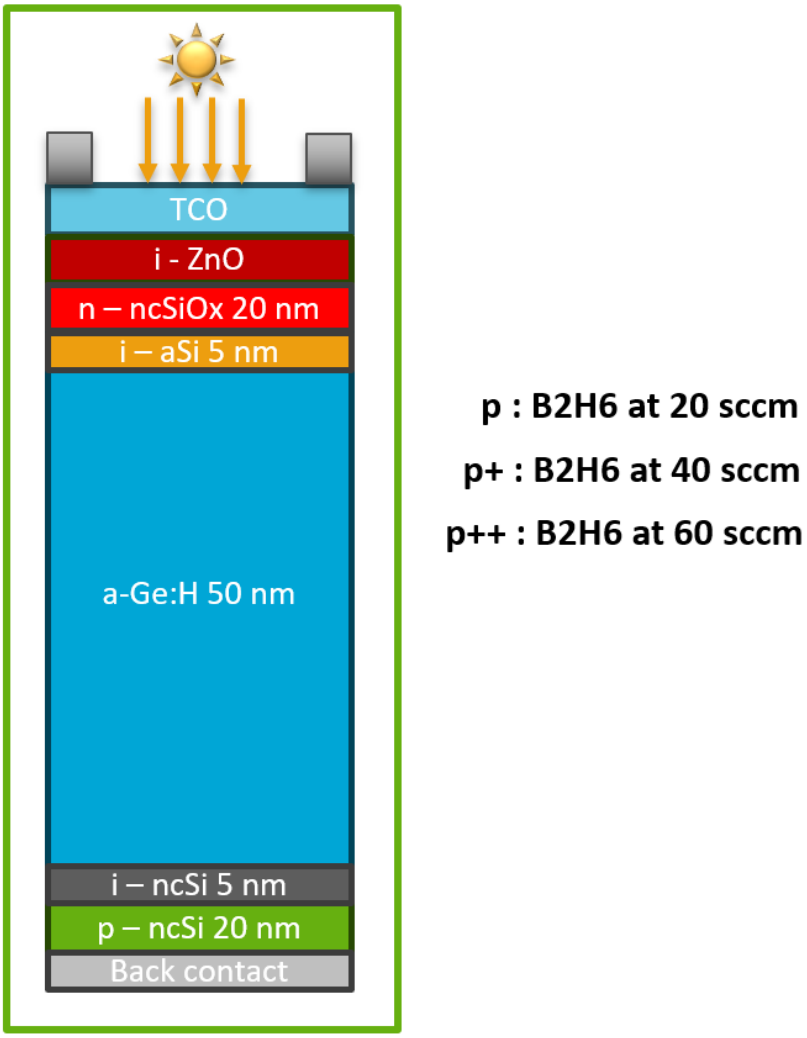


Figure 4.30: n-i-p configuration solar cell with varied doped p-layers

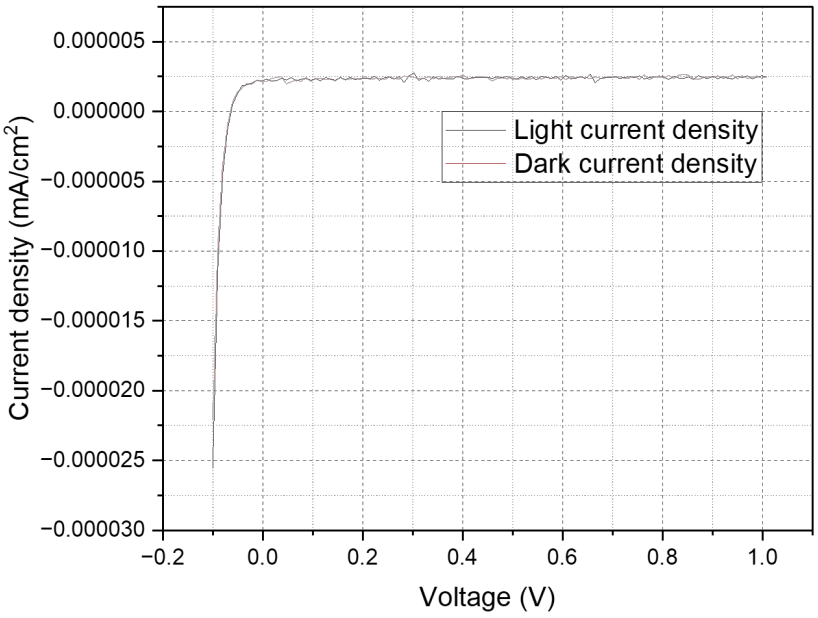


Figure 4.31: J-V characteristic of the p-doped solar cells

Despite changing the dopant concentration of the p-layer it is seen that the device doesn't display solar cell characteristics and the current density of the device is very minimal with breakdown voltage at -0.1 V. The reason that the cells deposited in the p-i-n configuration have shown solar cell characteristics but not the one deposited in n-i-p configuration is speculated to be due to better hole collection in p-i-n structures which can be advantageous for a-Ge:H absorbers that have lower hole mobilities than a-Si:H. Another reason could be due to lower recombination at the window layer in comaprison to the n/i interface in n-i-p cells [93], [86].

4.2.2. Device stability

Given the issues that were faced in this thesis while trying to optimize the Ge single junction solar cell, it was speculated that there might be a component of stability playing a role in these structures. Therefore, the cell given in Figure 4.26 with a 300 nm absorber was remeasured to check whether the cell was reproducible and if it showed the same behaviour.

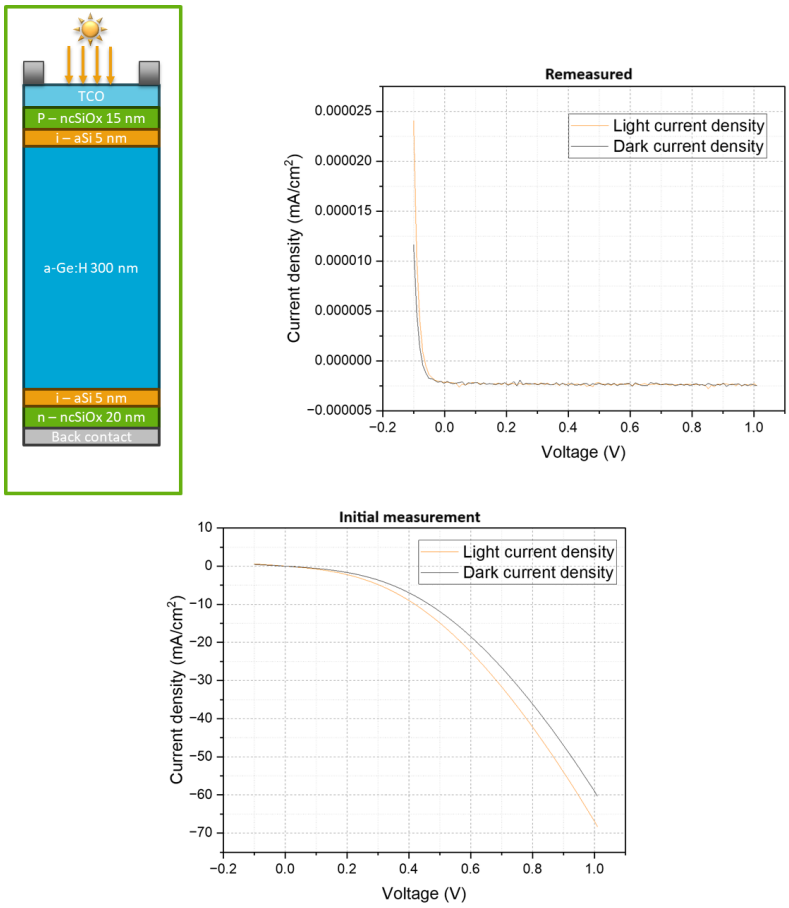


Figure 4.32: Stability measurement of the p-i-n configuration solar cell; top right : remeasured; bottom : Initial result

Figure 4.32 shows the JV characterisitc of the cell after 3 days in storage under vacuum with the above one being the remeasured and the bottom one being the previous result. It was observed that the cell did not display similar characteristics which raised questions about the stability of the intrinsic layer. These questions are addressed in this section.

The current density of the p-i-n configuration solar cell with an absorber layer of 150 nm was remeasured at a bias voltage from -0.01 V to 0.5 V. The cell architecture is the same as the one shown in Figure 4.26. In this case it was observed that the J-V characteristics remain the same whch is shown in Figure 4.33. Upon remeasuring the sample at the same bias voltages -0.1 to 1 V which was speculated to destroy the cells it was found that the cell was still showing the same J-V characteristic as before, which is completely different behaviour

from the remeasured sample in Figure 4.32.

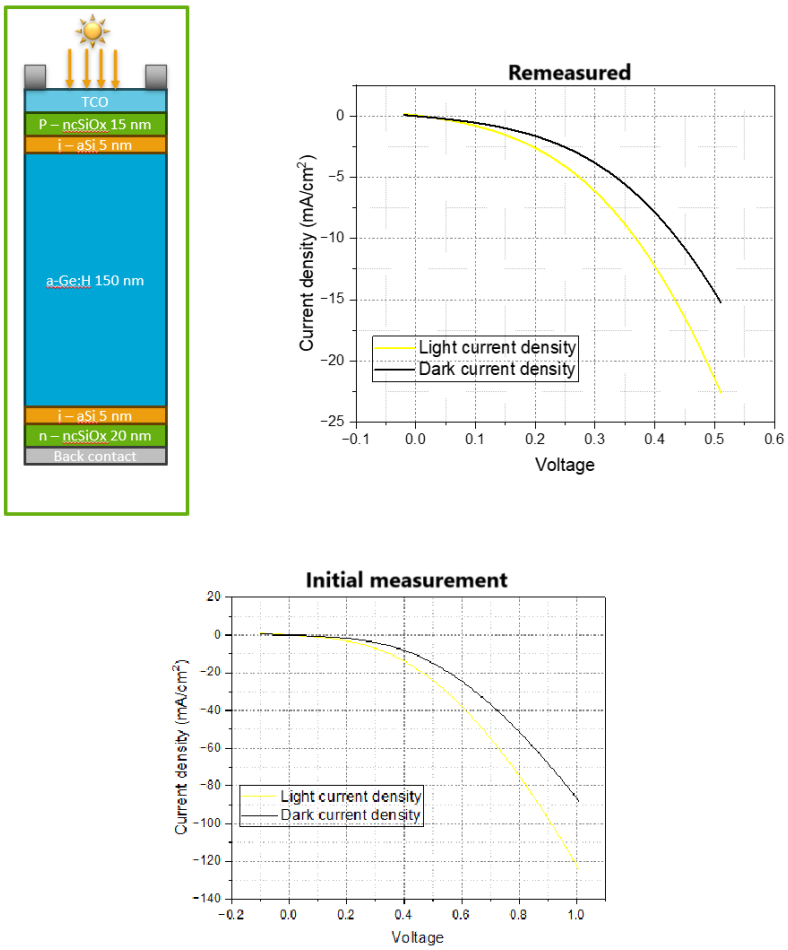


Figure 4.33: Stability measurement of the p-i-n configuration solar cell with 150 nm absorber

As shown in the previous section that despite altering the buffer layers, dopant concentration of the p layer, thickness of the germanium layer and hydrogen treatment of the germanium layer there was no behaviour that would suggest solar cell characteristics. This led to further scrutinizing of the Germanium layer. It was under the likelihood that there was a shift in the state of the germanium from amorphous to crystalline. This assumption was also unlikely as germanium can not convert from amorphous to germanium without the influence of external factors. To investigate on this impression Raman spectroscopy was carried out. This measurement identifies the intensity of the vibration modes. This measurement was carried out on both the Germanium layer which was deposited on a glass substrate and

on the Germanium layer which was deposited on the cell. Both germanium films were deposited at a pressure and power of 4.5 mbar and 12 W, respectively. The comparison of the Raman spectroscopy measurements for this sample are presented in Figure 4.34.

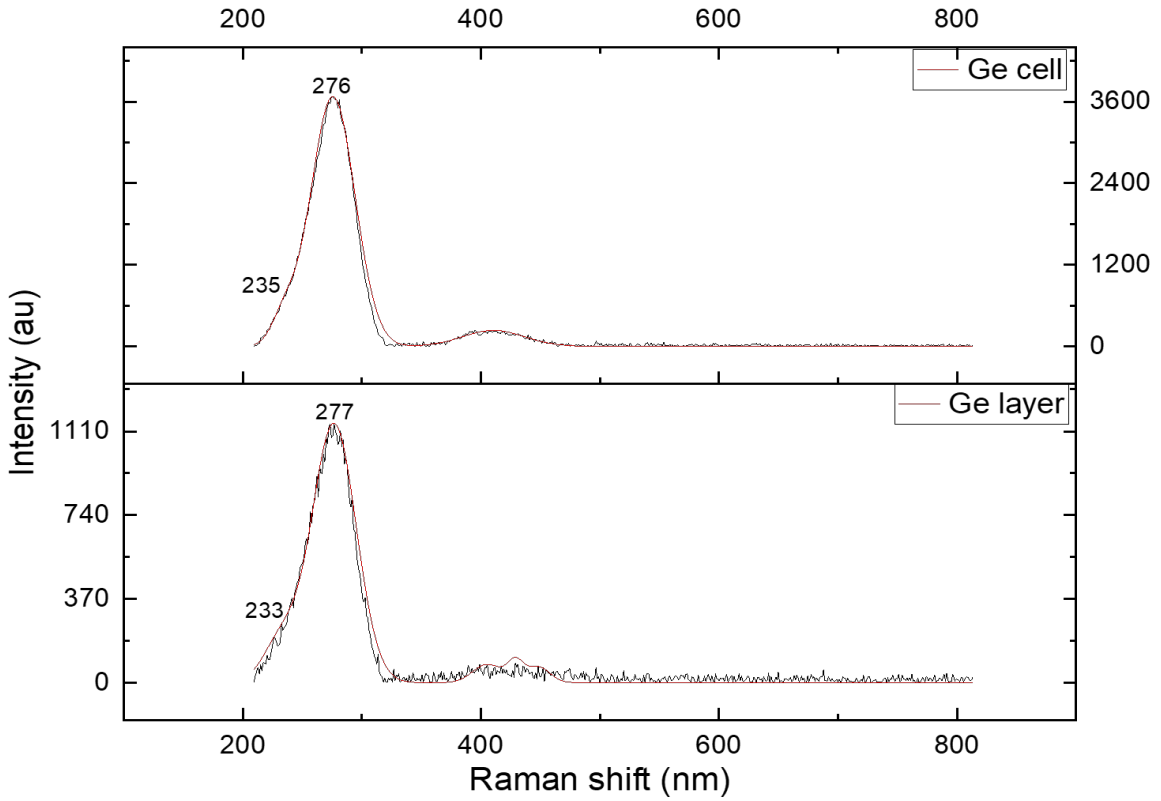


Figure 4.34: Raman spectroscopy of the germanium layer and solar cell deposited at 4.5 mbar and 12 W

Upon comparing the results it can be seen that there is no change in the composition of Germanium. The stretching modes of amorphous Germanium at 230-235 cm^{-1} and 275-280 cm^{-1}. The c-Ge peak at 300 cm^{-1} was not seen in any of the samples suggesting that the material is amorphous. A very small peak at around 410 cm^{-1} is also observed. Amorphous materials often exhibit a broad range of vibrational modes due to the lack of long-range order. A peak at 410 cm^{-1} could be associated with localized vibrational modes that are not present in crystalline germanium [94] [19]. The presence of impurities or defects in the amorphous germanium could introduce additional vibrational modes, leading to peaks that are not typically observed in pure amorphous germanium. These could include oxygen, hydrogen, or other elements that might be incorporated during the deposition process [94]

[95]. As Raman spectroscopy highlights the structural characteristics, a detailed look had to be taken into the composition of the amorphous germanium. Two germanium samples, which were deposited on the silicon wafers at a power and pressure of 4.5 mbar and 12 W, respectively were stored with exposure to the ambient air for a period of two weeks. The germanium layers are usually stored in a vacuum sealed box inside the clean room facility at TU Delft. The comparisons of the Germanium layers deposited at 4.5 mbar and 12 W before and after exposure to the ambient air have been shown in Figure 4.35.

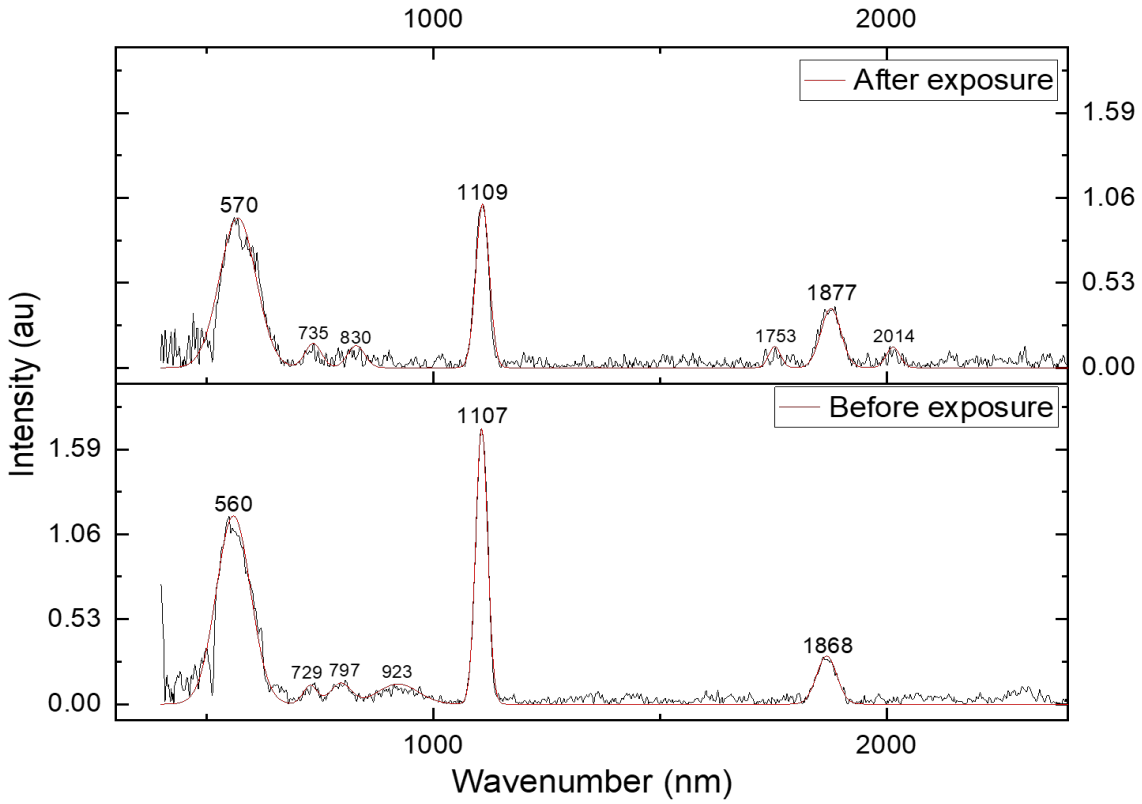


Figure 4.35: Comparison of the samples deposited at 4.5 mbar and 12 W before and after exposure to ambient air

From Figure 4.35 it can be seen that even after exposing the sample to the ambient surroundings there is no change in the material characteristics. The small changes that are observed are due to changes in measurement conditions such as the amount of time the sample was purged in nitrogen and the spot on the sample where the measurements are taken.

Additional experimentation is required to look into the material characteristics of the amor-

phous germanium and the interaction of the layers of the cells with each other.

5

Conclusion and Recommendations

5.1. Conclusion

The goal of this study was to produce and characterize hydrogenated germanium films for use as a low bandgap intrinsic absorber layer in p-i-n solar cells. The films are deposited using PECVD. Three research questions were established at the outset of this study. These are addressed one-by-one.

How do the deposition parameters affect the properties of the amorphous germanium layer?

The investigation of the deposition parameters was undertaken by depositing germanium layers to find the optimum regime for obtaining intrinsic films. The films produced were amorphous. The conditions that were varied were temperature, germane flow, pressure and power. Power was further investigated at a constant pressure of 3 mbar. It was found that intrinsic films were found from the region of 3 to 4.5 mbar at a power of 12 to 20 W respectively. The optimum germane flow was found to be at 3 sccm, while high temperatures of 225 and 275 °C produces intrinsic films of highest qualities.

How do material characteristics affect the opto-electrical properties of the germanium layers?

The characteristics of the samples were also looked into to observe its impact on the films. All of the films that were deposited showed a LSM which indicates small voids in the material which were also observed in previous studies carried out in the research group. These small voids potentially affect the band-gap by affecting the density of states. With an increase in power there is an increase in impurities in the sample that affect the activation energy and band-gap of the material.

What is the impact of the device architecture on the properties of the solar cell?
Upon finding a stable regime to deposit germanium films, the processing conditions were utilised to deposit the intrinsic layer of the solar cells. The cells were deposited in a p-i-n configuration which displayed solar cell characteristics with a ncSiO$_x$ p and n layer and an aSi buffer layer. The current density showed an increase with decrease in thickness. When the cells were deposited in n-i-p configuration with variations in the doping of the p layer there was no variation in the current density which was very small. When the J-V curve measurements were once again taken for the p-i-n configuration solar cell, the cell did not display solar cell characteristics.

5.2. Recommendations

The research has demonstrated the procedure to produce and characterize intrinsic hydrogenated germanium films. However, several steps in the process could be improved for better characterization and processing of films, making them suitable as low bandgap material. The recommendations for future research are covered in this chapter.

Firstly, some parameters in the processing could be explored further to optimize the film properties.The samples that were deposited apart from the temperature experiment were all deposited at 275 °C with variations in pressure, power and germane flow. There could be further experimentation with variations in pressure, power and germane flow at 225 °C too. Another parameter that can be further explored is the germane content. The effect of germane flow should be tested out by depositing at 3 mbar 20 W too as samples deposited at this pressure and power were intrinsic and reproducible too.

Additionally, the optimum regime for depositing reproducible germanium cells was explored, but when integrated with the cell, the cell did not depict the desired behaviour

and results. Thus, future research should experiment with very thin layers of amorphous germanium and other p layers and buffer layers. As the interactions between the various layers could not be studied, a measurement technique needs to be utilised which can do so. As with the cells deposited in n-i-p configuration, only the p layers had different variations of doping, experiments can be carried out by further doping the n layers. Furthermore, cells deposited at lower temperatures in various configurations should also be deposited.

Lastly, the ideal voltages at which the cells must be measured should also be looked into to get an understanding whether external factors are effecting the cell or the post deposition material properties.

Bibliography

[1] National Renewable Energy Laboratory (NREL), "Research on solar energy," 2024. Accessed: 2024-08-20.

[2] H. Matsumoto, T. Kiyobayashi, Y. Miyazaki, K. Watanabe, Y. Takao, T. Hibino, T. Kudo, and E. Abe, "Nanostructured pt/nb_2o_5 hybrid catalysts for polymer electrolyte fuel cells," *NPG Asia Materials*, vol. 2, pp. 70–77, 2010.

[3] J.-K. Choi and V. Fthenakis, "Crystalline silicon photovoltaic recycling planning: macro and micro perspectives," *Journal of Cleaner Production*, vol. 66, pp. 443–449, 2014.

[4] A. Shah, P. Torres, R. Tscharner, N. Wyrsch, and H. Keppner, "Photovoltaic technology: The case for thin-film solar cells," *Science*, vol. 285, no. 5428, pp. 692–698, 1999.

[5] Y. Wang, I. Ahmad, T. Leung, J. Lin, W. Chen, F. Liu, A. M. C. Ng, Y. Zhang, and A. B. Djurišić, "Encapsulation and stability testing of perovskite solar cells for real life applications," *ACS Materials Au*, vol. 2, no. 3, pp. 215–236, 2022.

[6] J. Geisz, R. France, K. Schulte, *et al.*, "Six-junction iii–v solar cells with 47.1% conversion efficiency under 143 suns concentration," *Nature Energy*, vol. 5, pp. 326–335, 2020.

[7] Wikipedia contributors, "Thin-film solar cell," 2024.

[8] EcoWatch contributors, "Thin-film solar panels," 2024.

[9] V. Muteri, M. Cellura, D. Curto, V. Franzitta, S. Longo, M. Mistretta, and M. L. Parisi, "Review on life cycle assessment of solar photovoltaic panels," *Energies*, vol. 13, no. 1, 2020.

[10] EE Power, "Tandem solar cells are breaking records." `https://eepower.com/tech-insights/tandem-solar-cells-are-breaking-records/#`. Accessed: 20-Aug-2024.

[11] J. Meier, J. Spitznagel, U. Kroll, C. Bucher, S. Fay, T. Moriarty, and A. Shah, "High-efficiency amorphous and "micromorph" silicon solar cells," in *3rd World Conference onPhotovoltaic Energy Conversion, 2003. Proceedings of*, vol. 3, pp. 2801–2805 Vol.3, 2003.

[12] S. Essig, C. Allebé, T. Remo, *et al.*, "Raising the one-sun conversion efficiency of III–V/Si solar cells to 32.8% for two junctions and 35.9% for three junctions," *Nature Energy*, vol. 2, p. 17144, 2017.

[13] T. de Vrijer, A. Ravichandran, B. Bouazzata, and A. H. Smets, "The impact of processing conditions and post-deposition oxidation on the opto-electrical properties of hydrogenated amorphous and nano-crystalline germanium films," *Journal of Non-Crystalline Solids*, vol. 553, p. 120507, 2021.

[14] Encyclopaedia Britannica, "Germanium," 2024. Accessed: 2024-08-20.

[15] V. Steenhoff, *Development of Amorphous Germanium Nanoabsorber Solar Cells*. PhD thesis, Carl von Ossietzky University of Oldenburg, Oldenburg, Germany, May 2016. Ph.D. dissertation.

[16] Y.-C. Yeo, X. Gong, M. J. H. van Dal, G. Vellianitis, and M. Passlack, "Germanium-based transistors for future high performance and low power logic applications," in *2015 IEEE International Electron Devices Meeting (IEDM)*, pp. 2.4.1–2.4.4, 2015.

[17] J. Tauc, R. Grigorovici, and A. Vancu, "Optical properties and electronic structure of amorphous germanium," *physica status solidi (b)*, vol. 15, no. 2, pp. 627–637, 1966.

[18] G. G. Pethuraja, R. E. Welser, A. K. Sood, C. Lee, N. J. Alexander, H. Efstathiadis, P. Haldar, and J. L. Harvey, "Effect of ge incorporation on bandgap and photosensitivity of amorphous sige thin films," *Materials Sciences and Applications*, vol. 3, no. 2, pp. 110–116, 2012.

[19] P. Liu, P. Longo, A. Zaslavsky, and D. Pacifici, "Optical bandgap of single- and multi-layered amorphous germanium ultra-thin films," *Applied Physics Letters*, vol. 107, no. 26, p. 261904, 2015.

[20] Y.-J. Kim, J.-H. Boo, B. Hong, and Y. J. Kim, "Effects of showerhead shapes on the flowfields in a rf-pecvd reactor," *Surface and Coatings Technology*, vol. 193, no. 1, pp. 88–93, 2005. Asian-European International Conference on Plasma Surface Engineering 2003.

[21] Energy Education, "Photovoltaic effect," 2024. Accessed: 2024-08-20.

[22] A. Luque and S. Hegedus, eds., *Handbook of Photovoltaic Science and Engineering*. Wiley, 2003.

[23] ResearchGate contributors, "Solar spectrum at the top of the atmosphere and at sea level." `https://www.researchgate.net/figure/Solar-spectrum-at-the-top-of-the-atmosphere-and-at-sea-level-1_fig1_271891094`, 2024. Accessed: 20-Aug-2024.

[24] Ossila, "The solar spectrum," 2024. Accessed: 2024-08-20.

[25] Wikipedia contributors, "Photon energy," 2024. Accessed: 2024-08-20.

[26] Wikipedia contributors, "Fermi level." `https://en.wikipedia.org/wiki/Fermi_level`, 2024. Accessed: 20-Aug-2024.

[27] A. Smets, K. Jäger, O. Isabella, R. Van Swaaij, and M. Zeman, *Solar Energy - The physics and engineering of photovoltaic conversion, technologies and systems*. 02 2016.

[28] I. García, M. Hinojosa, I. Lombardero, L. Cifuentes, I. Rey-Stolle, C. Algora, and A. Johnson, "Ge virtual substrates for high efficiency III-V solar cells: Applications, potential and challenges," in *2019 IEEE 46th Photovoltaic Specialists Conference (PVSC) Proceedings*, IEEE, 2019.

[29] P. Palleti, P. Seyidov, A. Gybin, *et al.*, "Properties of a highly compensated high-purity germanium," *Journal of Materials Science: Materials in Electronics*, vol. 35, p. 57, 2024.

[30] R. F. Pangestu, Z. M. Latif, and R. Ramli, "Research on coated and uncoated carbide cutting tool in turning stainless steel 304," *Applied Mechanics and Materials*, vol. 761, pp. 341–345, 2015.

[31] Delft University of Technology, "Solar energy course transcript - week 4," 2016.

[32] ResearchGate contributors, "Ge band structure with indirect bandgap." https://www.researchgate.net/figure/Ge-band-structure-with-indirect-bandgap_fig2_271706014, 2024. Accessed: 20-Aug-2024.

[33] M. Yamaguchi, "Iii–v compound multi-junction solar cells: present and future," *Solar Energy Materials and Solar Cells*, vol. 75, no. 1, pp. 261–269, 2003. PVSEC 12 Part II.

[34] LibreTexts, "Electron-hole recombination," 2024. Accessed: 2024-08-20.

[35] DelftX, "Recombination types: Shockley-read-hall," 2017. Accessed: 2024-08-20.

[36] Cadence Design Systems, "The types of recombination in semiconductors," 2022. Accessed: 2024-08-20.

[37] J. Meier, J. Spitznagel, U. Kroll, C. Bucher, S. Fay, T. Moriarty, and A. Shah, "High-efficiency amorphous and "micromorph" silicon solar cells," vol. 3, pp. 2801 – 2805 Vol.3, 06 2003.

[38] Fraunhofer Institute for Solar Energy Systems ISE, "Fraunhofer ise develops the world's most efficient solar cell with 47.6 percent efficiency," 2022. Accessed: 2024-08-20.

[39] N. Sato, M. Kondo, and H. Fujiwara, "Current-matched triple-junction solar cell design for enhanced efficiency," *Applied Physics Letters*, vol. 94, no. 22, p. 223504, 2009.

[40] J. Pastuszak and P. Węgierek, "Photovoltaic cell generations and current research directions for their development," *Materials*, vol. 15, no. 16, p. 5542, 2022.

[41] J Lanka Technologies, "Generations of solar cells." https://www.jlanka.com/generations-of-solar-cells/, 2024. Accessed: 20-Aug-2024.

[42] Solar Facts and Advice, "Solar cells: How they work and their types." https://www.solar-facts-and-advice.com/solar-cells.html, 2024. Accessed: 20-Aug-2024.

[43] H. Wu, X. Li, and L. Zhang, "Advancements in perovskite solar cells: A comprehensive review," *RSC Advances*, 2023.

[44] J. D. Smith, E. M. Brown, and A. L. Johnson, "Impact of diet on gut microbiota: A review of health benefits," *Frontiers in Microbiology*, vol. 13, p. 9414585, 2022.

[45] Ossila, "Radiative efficiency limit." `https://www.ossila.com/pages/radiative-efficiency-limit`. Accessed: 20-Aug-2024.

[46] G. Ahmad, G. Das, and J. Roy, "Performance and stability improvement of single junction a-si:h solar cell by interface engineering," *Journal of Materials Science: Materials in Electronics*, vol. 30, 07 2019.

[47] I. Massiot, *Design and fabrication of nanostructures for light-trapping in ultra-thin solar cells*. PhD thesis, 10 2013.

[48] N. Mavrikakis, "Nanostructured electrodes for thin-film silicon solar cells," 2012. Accessed: 2024-08-20.

[49] A. Cuevas, "The recombination parameter j0," *Energy Procedia*, vol. 55, 12 2014.

[50] B. Liu, L. Bai, X. Zhang, C. Wei, Q. Huang, J. Sun, H. Ren, G. Hou, and Y. Zhao, "Fill factor improvement in pin type hydrogenated amorphous silicon germanium thin film solar cells: Omnipotent n type μc-siox:h layer," *Solar Energy Materials and Solar Cells*, vol. 140, pp. 450–456, 2015.

[51] Y. Zhao, "Contact stack evaluation for shj solar cells and process development of ibc-shj solar cells," master's thesis, Delft University of Technology, 2018. Faculty of Electrical Engineering, Mathematics and Computer Science.

[52] C.-Y. Liu, J. T. Smith, and E. Brown, "Density of amorphous germanium films by x-ray reflectometry," *Journal of Vacuum Science & Technology A*, vol. 4, no. 3, pp. 577–582, 1986.

[53] J. W. Lee, S. H. Kim, and D. W. Park, "Influence of oxygen incorporation on the structural and electrical properties of silicon nitride films," *Applied Physics Letters*, vol. 62, no. 16, pp. 1961–1963, 1993.

[54] V. Sorianello, L. Colace, G. Assanto, and M. Nardone, "Micro-raman characterization of germanium thin films evaporated on various substrates," *Microelectronic Engineering*,

vol. 88, no. 4, pp. 492–495, 2011. Post-Si-CMOS electronic devices: the role of Ge and III-V materials.

[55] G. Lucovsky, S. S. Chao, J. Yang, J. E. Tyler, R. C. Ross, Czubatyj, and W., "Chemical bonding of hydrogen and oxygen in glow-discharge–deposited thin films of a-ge:h and a-ge:(h,o)," *Phys. Rev. B*, vol. 31, pp. 2190–2197, Feb 1985.

[56] S. University, "Low-temperature synthesis of polycrystalline semiconductor thin films on amorphous substrates," 2023. Accessed: August 24, 2024.

[57] W. Paul, "Structural, optical and photoelectronic properties of improved pecvd a-ge:h," *Journal of Non-Crystalline Solids*, vol. 137-138, pp. 803–808, 1991.

[58] D. Sharma, "Processing and characterization of novel low bandgap ge alloys for pv applications: Path towards a new generation of high-efficiency pv devices," master's thesis, Delft University of Technology, 2023.

[59] I. M. Mathews, "Refractive index and density," *Journal of the Franklin Institute*, vol. 177, no. 6, pp. 673–686, 1914.

[60] D. Mergel and M. Jerman, "Density and refractive index of thin evaporated films," *Chinese Optics Letters*, vol. 8, pp. 67–72, 04 2010.

[61] Z. Remeš, M. Vaněček, P. Torres, U. Kroll, A. Mahan, and R. Crandall, "Optical determination of the mass density of amorphous and microcrystalline silicon layers with different hydrogen contents," *Journal of Non-Crystalline Solids*, vol. 227-230, pp. 876–879, 1998.

[62] G. G. Politano and C. Versace, "Spectroscopic ellipsometry: Advancements, applications and future prospects in optical characterization," *Spectroscopy Journal*, vol. 1, no. 3, pp. 163–181, 2023.

[63] The Editors of Encyclopaedia Britannica, "Activation energy," 2021. Accessed: August 25, 2024.

[64] B. G. Streetman and S. Banerjee, *Solid State Electronic Devices*. Upper Saddle River, NJ: Pearson Prentice Hall, 6th ed., 2006.

[65] S. Johnston, "Advanced concepts for high-efficiency crystalline silicon solar cells," 2014. Accessed: 2024-08-20.

[66] A. Brown and J. Smith, "Bismuth selenide (bi_2se_3)," in *Landolt-Börnstein - Group III Condensed Matter*, Springer, 2005. Accessed: 2024-08-20.

[67] J. Zhou, J. Tang, Q. Liu, and Y. Zhang, "Nanostructures for enhanced light trapping in thin-film solar cells," *Nanoscale Research Letters*, vol. 2, no. 11, pp. 577–584, 2007.

[68] A. Y. Kovalevsky, B. L. Hanson, S. A. Mason, and M. P. Blakeley, "Diber: A program for the automated detection of regions of interest in protein crystals," *Journal of Applied Crystallography*, vol. 43, no. 6, pp. 1505–1511, 2010.

[69] W. Paul, "Structural, optical and photoelectronic properties of improved pecvd a-ge:h," *Journal of Non-Crystalline Solids*, vol. 137-138, pp. 803–808, 1991.

[70] T. de Vrijer, J. E. van Dingen, P. J. Roelandschap, K. Roodenburg, and A. H. Smets, "Improved pecvd processed hydrogenated germanium films through temperature induced densification," *Materials Science in Semiconductor Processing*, vol. 138, p. 106285, 2022.

[71] J. I. Pankove and D. A. Kiewit, "Optical processes in semiconductors," *Journal of The Electrochemical Society*, vol. 119, p. 156Ca, may 1972.

[72] M. Guo, H. He, K. Yi, S. Shao, G. Hu, and J. Shao, "Optical characteristics of ultrathin amorphous ge films," *Chinese Optics Letters*, vol. 18, p. 103101, 10 2020.

[73] D. G. Thomas and J. J. Hopfield, "Deep centers in gallium arsenide and gallium phosphide detected by optically detected magnetic resonance," *physica status solidi (b)*, vol. 115, no. 1, pp. 11–35, 1983.

[74] S. Yamamoto, Y. Shigesato, and S. Hikosaka, "Low-temperature fabrication of polycrystalline silicon thin films by metal-induced crystallization," *Japanese Journal of Applied Physics*, vol. 31, no. 6R, pp. 1730–1735, 1992.

[75] J. L. Andujar, E. Bertran, A. Canillas, C. Roeh, and J. L. Morenza, "Influence of pressure and radio frequency power on deposition rate and structural properties of hydrogenated amorphous silicon thin films prepared by plasma deposition," *Journal of Applied Physics*, vol. 70, pp. 489–493, September 1991.

[76] B. Staebler, "Tuning the bandgap of an amorphous sputtered germanium photovoltaic cell," master's thesis, University of Louisville, May 2012.

[77] T. Böckendorf, J. Kirschbaum, F. Kipke, D. Bougeard, J. L. Hansen, A. N. Larsen, M. Posselt, and H. Bracht, "Experimental and theoretical studies on self-diffusion in amorphous germanium," *Journal Name*.

[78] J. Lee, J. Shin, and k. s. Lim, "Thin film silicon solar cells on zno/sno2/glass substrate," *ECS Transactions*, vol. 1, 07 2006.

[79] D. J. Lockwood and J.-M. Baribeau, "Quantum confinement in si and ge nanostructures," *APL Materials*, vol. 1, no. 1, p. 011302, 2021.

[80] B. Abeles and T. Tiedje, "Amorphous semiconductor superlattices," *Phys. Rev. Lett.*, vol. 51, pp. 2003–2006, Nov 1983.

[81] B. Abeles, "Amorphous semiconductor superlattices," *Superlattices and Microstructures*, vol. 5, no. 4, pp. 473–480, 1989.

[82] B. Abeles and T. Tiedje, "Electrical transport in amorphous hydrogenated germanium films," *Applied Physics Letters*, vol. 49, no. 10, pp. 569–571, 1986.

[83] E. A. Schiff, *Low-Mobility Solar Cells: A Device Physics Primer with Application to Amorphous Silicon*. Springer, 2003.

[84] D. A. B. Miller, D. S. Chemla, S. Schmitt-Rink, A. C. Gossard, and W. Wiegmann, "Quantum shift of the optical absorption edge in quantum wells," *Applied Physics Letters*, vol. 51, no. 4, pp. 264–266, 1987.

[85] H. Meddeb, N. Osterthun, M. Götz, O. Sergeev, K. Gehrke, M. Vehse, and C. Agert, "Quantum confinement-tunable solar cell based on ultrathin amorphous germanium," *Nano Energy*, vol. 76, p. 105048, 2020.

[86] S. Wieder, "Amorphous silicon solar cells: Comparison of p-i-n and n-i-p structures with zinc-oxide frontcontact," tech. rep., Institut für Schicht- und Ionentechnik. Technical Report.

[87] M.-T. Antonio, "The resistor and its respective characteristic curve incorporating the curve of maximum power," 2020. Accessed: 2024-08-20.

[88] Huasun Solar, "The role of passivation layers in hjt solar cells and their impact on device performance," 2023. Accessed: 2024-08-20.

[89] Clean Energy Business Council, "Solar cell passivation," 2024. Accessed: 2024-08-20.

[90] H. H. Wieder, "The influence of interface and near-interface traps on the generation and recombination properties of silicon mos devices," Technical Report Jülich Report 3721, Forschungszentrum Jülich, 2000. Accessed: 2024-08-20.

[91] W. Böttler, J. Hupkes, and H. Stiebig, "Window layer for high-efficiency n-i-p solar cells," in *Proceedings of the 25th European Photovoltaic Solar Energy Conference and Exhibition*, pp. 3472–3476, 2010. Accessed: 2024-08-20.

[92] M. U. Halbich, D. Zielke, R. Gogolin, J. Schmidt, and B. Rech, "Improved surface passivation and reduced parasitic absorption in pedot:pss/c-si heterojunction solar cells through the admixture of sorbitol," *Scientific Reports*, vol. 9, p. 9775, 2019.

[93] P. Jelodarian and A. Kosarian, "Effect of p-layer and i-layer properties on the electrical behaviour of advanced a-si:h/a-sige:h thin film solar cell from numerical modeling prospect," *Energy Reports*, vol. 7, pp. 1755–1764, 2021.

[94] E. Hüger, F. Strauß, J. Stahn, J. Deubener, M. Bruns, and H. Schmidt, "In-situ measurement of self-atom diffusion in solids using amorphous germanium as a model system," *Scientific Reports*, vol. 8, p. 17722, 2018.

[95] A. names if available, "Properties of amorphous germanium films,"